Formal reply to GMD-2020-150

First, the authors would like to thank all the reviewers and editors for their assistance in the manuscript review process. Based on the comments of two anonymous Reviewers and our own consideration of improving this work, we have largely revised the initial version/preprint. The major changes are listed as follows. Detailed responses to each Reviewer are attached. We use the black font to indicate comments and questions by two Reviewers, and blue for our response. The italic font describes how the manuscript has been modified.

Major revision

1. Both reviewers suggested to give more details on the explicit diffusion option and to demonstrate its impact. As mentioned in the short reply to Reviewer#1, we have revised the configuration of explicit diffusion based on some further exploration and tests. In the initial preprint, the Smagorinsky diffusion with a mean length scale was used. In this version, the square of this mean length is replaced by the length product of two local crossing edges. This leads to several changes in the simulations: (i) the sensitivity to the Smagorinsky coefficient is reduced, now closer to the QU simulations; (ii) given the same Smagorinsky coefficient, the tropical cyclone magnitude increases as compared to the initial version, because the diffusion strength in the fine-resolution area is reduced. *More details have been elaborated in the main text (Section 2.3.1).* Smagorinsky is not used for tracer transport in this version, although the sensitivity due to this is limited. Meanwhile, a fourth-order hyperdiffusion for the horizontal velocity is activated. Its reference coefficient has been scaled. Activating this option is helpful in both pure dynamical core tests and moist physics tests. *The reasons have been elaborated in the revised manuscript (Section 2.3.2).*
2. *We have rerun all the experiments in this manuscript version based on this latest configuration.* The simulations are further improved due to the above mentioned modifications. The model code and running scripts have been updated as a reference. Thanks to the open interactive discussion of GMD, the preprint provides a basis for the discussion in this revision. The readers may also compare the results of this version with those in the preprint to clearly see the difference.
3. *We have presented a full-physics variable-resolution test.* This helps to examine the VR behavior under more complex nonlinear feedback. It mainly examines three issues:
   (i) using explicit diffusion (hyperdiffusion only, Smagorinsky + hyperdiffusion) only slightly diffuses the key physical object;
   (ii) using explicit diffusion can suppress generation of some highly unrealistic disturbances found in full-physics modeling, which are far away from the initial vortex (the refined region);
   (iii) providing a comparison of two grids: G6B3X16L4 and G6B3X16. G6B3X16 has more rapid resolution changes. This helps to examine whether a high-densification ratio may seriously harm the simulation.
4. In the initial version, the relative vorticity field in the main text is displayed on the raw triangular grid that defines vorticity. As mentioned, this will show some oscillations that actually reflect the mesh shape, not real errors. To avoid aliasing, *we have remapped the vorticity field to the Voronoi cell.* This remapping is used for both QU and VR results in the main text.
5. *We have thoroughly improved the language of this manuscript. Most of the main text has been reorganized and rewritten. The marked-up manuscript version is presented in all-blue mode.*

   The current structure of this manuscript is organized as follows.

1. Introduction

   We have further emphasized the importance and value of VR modeling, more specifically, the multiresolution approach supported by an unstructured mesh model. Two major challenges of VR modeling have been further elaborated: to resolve the fine-scale fluid structures; to avoid adverse impacts due to mesh transition and the higher solution errors in the coarse-mesh region.

2. Model description

   We have provided a broader introduction on the model framework, dynamics, physics packages. In particular, a detailed description about the choice and configuration of the explicit diffusion options (Smagorinsky and hyperdiffusion) is given.

3. Mesh generation

The presentation has been improved. Figures 1 and 2 are used for an illustration.

4. Dry atmosphere

The results are improved. Figures 3,4 focus on the fine-scale resolving ability, and the performance over the mesh transition zone. Figures 5,6,7 focus on the issue of solution errors, with a more detailed analysis. Figure 8 focus on multiregional VR modeling, and reveal the impact of activating the hyperdiffusion option.

5. Moist atmosphere

5.1 Simple physics

Figures 9,10,11 focus on the impact of varying the mesh-generation parameters. The results are improved and a more detailed analysis has been given. Figure 12 offers a comparison of two QU-VR groups, focusing on resolution sensitivity.

5.2 Full physics

Figures 13, 14 focus on the overall performance and the impacts of explicit diffusion. Figure 15 focuses on the impact of different mesh styles.

6. Summary

(i) The overall performance.

(ii) The impact of explicit diffusion.

(iii) The impact of the mesh styles.

Author note: The attached comments of two reviewers are copied from their PDF files. Some typos and format errors may exist during the transfer process.

Reviewer#1: Review of 'Configuration and Evaluation of a Global Unstructured Mesh Model based on the Variable-Resolution Approach'

In this manuscript, the variable-resolution (V-R) version of the GRIST model, based on Voronoi tessellations is described. The authors define the mesh generation process and explore multiple refinement approaches with a dry dynamical core test case (the Jablonowski-Williamson baroclinic wave) and a moist test case with simplified physics (the Reed-Jablonowski tropical cyclone). They subjectively (visually) and objectively (l2 errors, etc.) compare V-R simulations against quasi-uniform (Q-U) reference simulations and verify the V-R simulations perform generally as one would expect, particularly based on previous findings with V-R models using similar test cases.

V-R models have indeed been shown to be useful tools and multiple modeling centers are currently pursuing their development. Therefore, further evaluation and validation of such configurations is warranted, especially as V-R models become more commonly used for scientific research and application.

In general, the results here are a confirmation of robust performance rather than any overtly new physical insight. This makes GMD a suitable venue for such work. I do find the manuscript fairly underdeveloped, however. The model description is lacking, particular describing options specific to V-R dynamical cores such as scale-specific diffusion and model timestep. The simulations evaluating the ability of the tropical cyclone to move between resolutions are interesting but feel almost tacked on, with weak expansive discussion, particularly with regard to diffusion behavior. Some other useful and commonly-reported information is also omitted, such as computational scaling numbers.

While the manuscript wasn't illegible by any means, it did contain numerous grammatical errors that detract at times from the science.

I suggest major revisions. Again, this is more of an application of existing test cases to an existing model to essentially demonstrate that a V-R configuration is not performing poorly. For this to be a useful reference to other users of GRIST in the future, as well as a comparison benchmark for other modeling centers, some additional evaluation and breadth of discussion is warranted.

Major comments

• The model description in Section 2 is lacking.

– For example, it is unclear exactly what numerics are being applied. Finite volume, I assume? What is the vertical discretization? How close are the numerics to the Model for Prediction Across Scales (MPAS)?

Reply: To address this concern, *we have provided more details in the model description (Section 2.1)*. As mentioned earlier in the short reply, GRIST used some well-established techniques available in the icosahedral-/Voronoi-mesh modeling community, based on some publicly available documents. These details can be clearly found in the previous model development studies. *We have concisely summarized them in this revision.* GRIST is a different model and has its own unique aspects. Therefore, while MPAS has already examined the VR performance based on the centroidal Voronoi tessellation, it is still important to do our own exploration.

– It seems reasonable that the timestep of a global V-R simulation scales with the finest grid spacing to satisfy the CFL constraint, although this isn't explicitly stated. It would be helpful to note this, however, as some ill-posed V-R configurations can actually be more restrictive from a stability perspective than their equivalent Q-U counterparts.

Reply: The current dycore timestep is mainly determined by the theoretical time step (e.g., we typically use an acoustic Courant number ~0.5 based on the smallest mean length scale, assume 350 m/s), although not all the tests use the maximum allowable step. The tracer transport and physics steps can be enlarged accordingly (e.g., DTP=1:5:10). The timestep for each test can be found in the supplement file.

We agree this comment very much: "some ill-posed V-R configurations can actually be more restrictive from a stability perspective…". *We have explicitly stated this issue in Section 2.3.* Actually, even for a QU model, a proper model configuration is also important, especially for high-resolution applications.

As mentioned, the fourth-order hyperdiffusion option of horizontal velocity has been activated. One of the reasons is that the Smagorinsky option needs a higher coefficient (as compared to uniform-mesh modeling) to suppress small-scale oscillations due to mesh transition in the VR mode, which in turn, restricts the numerical stability (especially the DTP splitting mode because diffusion is called at the step of physics). A background hyperdiffusion is more effective in suppressing these small-scale oscillations. The Smagorinsky scheme, even with a higher coefficient, can be inactive for certain regions. With hyperdiffusion, we can use a moderate Smagorinsky coefficient that does not challenge the stability, even in the tests using a highly variable mesh that may reach sub-10 km locally. *This has been added in the revised manuscript. (see Section 2.3.1, 2.3.2)*

– What is the vertical resolution of the model? Is this constant across all configurations, or correspondingly increased in either/both the V-R and higher-resolution Q-U runs? How does this compare to other models with published baroclinic wave and tropical cyclone test results?

Reply: Indeed, some studies suggested that the vertical resolution should increase with increasing horizontal resolution, but we have not considered the impact of vertical resolution. In all our tests, we use 30 full vertical levels that are basically identical to the CAM5 setup used by Reed and Jablonowski (2012; 10.1029/2011MS000099). This was also used in our earlier QU model tests. A similar 30-level setup was used by Gettelman et al. (2018; 10.1002/2017MS001227) and Zarzycki et al. (2014; 10.1175/MWR-D-13-00179.1) in their CAM-SE-VR modeling. Thus, the simulations in this work can be compared with these earlier studies given the same horizontal resolution. *We have mentioned the vertical resolution in the revision. (Section 2.1, the last paragraph)*

– Appealing aspects of V-R modeling are the computational savings when solving a regional problem. Do the authors have scaling numbers that could provide a more objective quantification of this? Should they expect the simulations to scale linearly with the number of degrees of freedom in the mesh? Is there additional overhead associated with refinement that causes this scaling to be sub-linear?

Reply: As mentioned, the time step is limited by the fine-resolution area (for the tests we have examined). Thus, compared to a fine-resolution uniform-mesh model, the VR model is definitely more economic as it reduces the total grid number. For the scaling issue, we have compared a pair of VR and QU grids (G6B3, G6B3X16L4, 368642 cells). These tests use the full-physics configuration described in the revised manuscript with the nonhydrostatic core. As shown in Figure 1 of this reply, the speed up ratios and parallel efficiency look similar (at least for this test). Note that some super-linear speedup ratios are found, we ascribe this to relatively inefficient cache access of indirect addressing when using a small number of cores. For more details about the parallel infrastructure, one may find in Liu et al. (2020, manuscript submitted to GMD).

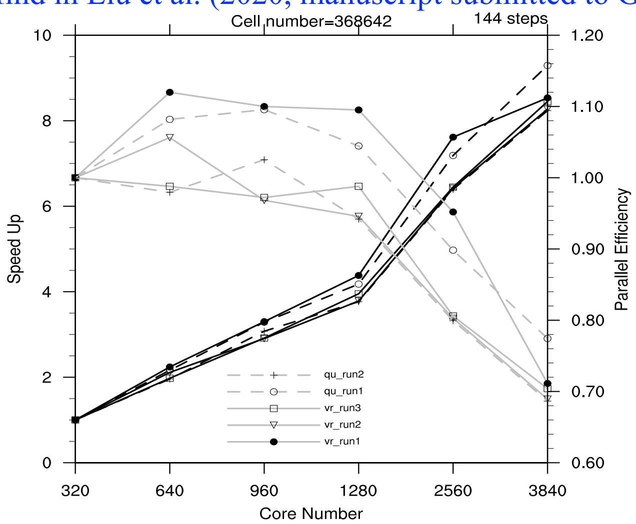

Figure1 Tropical cyclone test with full physics: speed up ratio and parallel efficiency for quasi-uniform (qu) and variable-resolution (vr) runs (NDC, G6B3, 368642 cells), starting from 320 cores to 3840 cores. Computing environment: Intel CPU E5-2697V4, 2.6GHz, 32 cores, 128 GB/node. Note that this test used a different cluster from that used by Zhang et al. (2020), and the scaling performance cannot be strictly compared. It only gives a relative comparison of QU and VR.

• Along this line, it is unclear what (if any) modifications are made for the V-R configurations relative to the Q-U. A Smagorinsky diffusion is applied in the horizontal. Is there any additional scale-selective explicit diffusion such as hyperdiffusion, or does the flow-dependent Smagorinsky handle everything? The latter would imply a fairly diffusive scheme in an implicit sense.

Reply: As replied above, in the initial preprint, only a Smagorinsky diffusion is applied in the horizontal. Again, we emphasize that the Smagorinsky diffusion is indeed stronger if fully active, but not that diffusive. For VR modeling, a background hyperdiffusion is more helpful to suppress grid-scale oscillations due to increased mesh discontinuity. *The detailed reasons have been added to the manuscript (Section 2.3.1, Section 2.3.2).*

• The moist tropical cyclone test section is underdeveloped.

– A couple sentences of additional description are warranted. What is the surface configuration, what does the idealized moist physics consist of? Convection? Boundary layer parameterization? Surface fluxes? How else is the model initialized?

Reply: *This information has been added in the revision. (Section 2.2)*

– The cyclone moves through the mesh – how is this done? Is there a background flow or does the configuration rely on beta drift associated with gradients of Coriolis across the cyclone?

Reply: *We have added necessary information when describing this test case. (the 1st paragraph of Section 5.1)*

– I would postulate that relative vorticity would be a better quantity to evaluate when assessing potential distortion or wave reflection in a numerical accuracy sense (e.g., Figs. 7-8). Are there artifacts in this field during the TC transit?

Reply: *We have shown the relative vorticity field of a TC case in the supplement file.* As you may see, there is no oscillation in this field. The vorticity field in this test is basically a mass of positive vorticity values, and does not show the fine-scale structure as in the baroclinic wave. So we do not include it in the main text.

– Other relevant citations which could help contextualize the TC results with respect to dynamical core and diffusion are Zhao et al. [2012] and Reed et al. [2015].

Reply: *These two references have been introduced in the main text to demonstrate the impact of model dynamics on the tropical cyclone simulations (the 2nd paragraph of Section5.1).*

• It is quite unclear exactly what the authors are showing in Fig. 12. Is the goal of this figure to show that V-R simulations are more sensitive to diffusion coefficient than a Q-U grid with the same setting(s)? In some ways, it is a natural finding that a cyclone transiting multiple grid spacing will 'feel' multiple diffusion scales, although as noted above, it isn't stated whether this diffusion explicitly scales with resolution or this is an implicit response. Further, in the abstract, the authors note that this 'suggest[s] the importance of parameter tuning,' although there is not enough description of the configuration to support this statement. Is this tuning just one 'number' for the whole mesh? I would recommend spending another paragraph or two explaining the importance of this finding in the context of the V-R validation exercise and how it pertains to the evaluated version of GRIST.

Reply: Thanks for this comment. As mentioned, the parametric sensitivity to the Smagorinsky coefficient has been largely reduced because a local-scale Smagorinsky eddy viscosity is used. The original formulation with a mean length scale implies stronger diffusion (than necessary) for the fine-resolution area. It also leads to higher stability restriction, especially when it comes to a high densification ratio (e.g., G6B3X16). *We have explicitly compared the scaled and unscaled formulation to demonstrate the impact of this scaling (see the last paragraph of Section 5.1 and the supplement file).*

• Is is unclear from the KE spectra how well the V-R runs are doing. For example, they could be accumulating spurious energy near the grid cell. It doesn't appear that they are from the spatial plots, however, the interpolation to the T106 Gaussian grid means nothing definitive can be said about the refined regions within the nests since those are below the truncation scale. There are a few ways to evaluate KE spectra within a regional model or regional patch, such as those proposed by Errico [1985] and Skamarock [2004]. I would recommend their exploration.

Reply: Thanks for this suggestion. *We have recomputed regional KE spectra (based on the new tests) over a selected regional domain using the discrete cosine transform (DCT) method. The* *related context has been modified.* The basic computational procedure has been given in the Appendix. *For KE spectra, we also performed additional tests to examine the impact of varying the reference hyperviscosity coefficient.*

Minor comments

• Lines 49-53. Wave reflection can be strongly influenced by other parameters than transition zone width, such as numerical method and grid staggering. See Ullrich and Jablonowski [2011].

Reply: *This information has been given in the introduction, used as a motivation.*

• It is unclear why both hydrostatic and non-hydrostatic cores are exercised here. Both test cases do not emphasize non-hydrostatic dynamics (being of relatively 'coarse' resolution compared to regional weather models), so it should be expected that both solutions look similar in the absence of some sort of erroneous formulation. There is nothing inherently wrong with testing both cores, although it is mentioned more frequently than probably necessary.

Reply: Indeed, the only reason of checking both cores is to verify their similarity and consistency at the hydrostatic regime. Such consistency is our expectation before performing these tests. Our earlier studies have confirmed this in the QU mode, so we expect that there is no abnormal behavior in the VR mode as well. Considering that this issue has been confirmed in the preprint, for the TC test, *only the nonhydrostatic core is experimented based on the latest configuration.* The readers may see the preprint for a reference.

• Section 2.2.2. is quite long, specific, and doesn't add a ton of 'added value' to the manuscript. I would recommend shortening this slightly; keeping the description of important parameters (e.g., γ, λ, etc.) and removing extraneous text.

Reply: Sorry for this. *We have reduced the content of this section (now Section 3.2).*

• Lines 192-193. Why is the iteration number different for these grid methods? Is there a quantitative reason, or was this a subjective design choice during mesh generation?

Reply: This is basically empirical. During the iteration, two criteria are used to stop the loop:
(i) reach a user-defined minimum iterative number;
(ii) the circumcenter of each triangle falls within its shape.

The formal check of criterion (ii) will only be activated after the minimum iterative number. In general, when more points are used, more iterative steps are required to meet the second criterion.

• I am not sure what this sentence means in the code and data availability section: 'GRIST is available at https://github.com/grist-dev, in private repositories. A way is provided for the editor and reviewers to access the code, which does not compromise their anonymity (to our best effort).' I would double-check that this all conforms to GMD's policies.

Reply: As mentioned earlier in the short reply, *we have modified some statements in the code and data part.* The code can be accessed publicly, while needs authorization.

• I believe both the baroclinic wave and tropical cyclone test case were part of the Dynamical Core Model Intercomparison Project (DCMIP) test suite. It may be worth reviewing multi-center reviews (such as Ullrich et al. [2017]) or references from other labs to see if there is any benefit in comparing results to those previously published using the same test cases.

Reply: *We have added this information (DCMIP) in the introduction. In the main text, we have provided the online link of DCMIP2016 to direct interested readers to this site.*

• Fig. 2. It is not 100% clear which (X4) mesh is being shown. Are all the V-R meshes so similar they functionally look like this? If they are not, the three different generator meshes should be plotted.

Reply: If one uses the same density function for mesh generation, the grids produced by different generators will look similar, but differ in detail. *We have replaced fig. 2 with the grids generated by three density functions used in this study.*

• Figs. 5, 8, and 9. Why do the black refinement isolines look 'jagged?' I assume the plotting software is struggling with cell areas right at a given threshold, would recommend smoothing for visualization.

Reply: Thanks for this suggestion. *We have smoothed the isolines of the cell size using the nearest neighboring average, with a repeating number 100.*

• Fig. 6. Recommend moving the reference slopes above the spectra so that they do not intersect the raw data.

Reply: Thanks for this suggestion. *Done.*

Typographical errors and grammar

As noted above, there are numerous – albeit generally minor – grammatical errors. This list is not meant to be exhaustive, but rather, a few obvious catches I noted while reading. I recommend a thorough proofread for grammar before resubmission.

• Line 37. ... while permitting...
• Line 43. ... while retaining or minimally degrading...
• Line 64. ... maintains tropical cyclones...
• Line 83. 'three difference initial point sets' is awkward phrasing.
• Line 95. ... developmental ... (?)
• Line 216. ... model level nearest to...
• Lines 232-233. 'Nevertheless...' sentence is awkward.
• Lines 252. Perhaps something like 'sign of the relative vorticity is flipped to account for hemispheric differences' or thereabouts.

Reply: *We have rewritten most of the main text, and carefully improved the language.*

Reviewer#2: Review of Configuration and Evaluation of a Global Unstructured Mesh Model based on the Variable-Resolution Approach Zhou et al.

General Impressions

This study evaluates the performance of the variable-resolution configuration of a newer global model GRIST, and seeks to understand the various strengths and weaknesses of different refinement meshes. The authors provide results from both dry and moist idealized experiments that illustrate that the solution in the refined regions resemble the uniform high-resolution solutions. While this take home message is clear, I would like to see further analysis/discussion on why the errors tend to be larger in VR compared with the uniform resolution runs, examples that I point out specifically in the comments section, and also how the Smagorinsky operators are implemented in VR. After addressing these minor revisions, I think this manuscript is acceptable for publication in GMD.

Comments

L64: CAM has multiple dycores, each with distinct numerical properties, and so this statement can be misleading. I think the authors should consider mentioning that the Zarzycki study cited used the spectral-element dycore.

Reply: *This information has been added in the revision (please see introduction).*

L88: This statement "[a] series of numerical tests was performed to examine the model reliability under more challenging conditions," reads like there are more challenging tests than the TC test-case, but the TC test-case is the most complex case used in this study.

Reply: Thanks. *This statement has been revised.*

L108: If I recall correctly, the Smagorinsky coefficients scale with grid spacing. Is the density function used to determine the Smagorinsky coefficients?

Reply: In this revised manuscript, we have used the product of local grid distances to replace the square of mean length scale in the Smagorinsky eddy viscosity. For the hyperdiffusion, its reference coefficient is scaled by the ratio of grid spacings. *The details have been given in Section 2.3.* When testing the scaled diffusion, we did experiment with the density function approach for evaluating the ratio, but this choice was not used in the production runs because we feel that this formulation relies on the theoretical relation between the density values and cell spacings.

Model and configurations: Can the authors include the number of vertical levels used in the simulations?

Reply: There are 30 full vertical levels used in all the numerical tests of this work. *This has been mentioned in the revised paper. (the last paragraph of Section 2.1)*

L160: The authors argue that the densification ratio should be no larger than 1:4, and point to a citation that I can't seem to get access to. I'm having trouble interpreting this statement. Do the authors mean no less than 1:4? Would this then mean the refined grid spacing should be no less than a 1/4 of the coarser region grid spacing? If so, I can think of many spectral-element VR studies that use a much smaller ratio without having reported any serious errors. I could be misunderstanding entirely here, but I think this densification ratio and implications of some lower limit should be spelled out more clearly for the general reader.

Reply: Liu and Yang (2017) is available at:
https://doc.global-sci.org/uploads/Issue/CiCP/v5n21/521_1310.pdf

Based on some MPAS-SW simulations of the 2D cosine bell advection and steady state shallow water flow (10242 and 40962 cells), they suggested that the densification ratio should better have a moderate value (e.g., 1:X, X<4). They showed that 1:2 or 1:3 overall generates smaller errors than 1:4. This was also shown in Ringler et al. (2011) that 1:4 indeed generates greater errors than 1:2, given the same coarse-mesh resolution (their Figure 8).

The implications of these results, based on our understanding, are not to discourage one from using a higher densification ratio (e.g., X16). The practical impact of these increased solution errors (e.g., from 1:2 to 1:4) may not be serious enough to deteriorate the practical simulations. MPAS simulations with 1:16 ratio available in the literature do not report any serious problem as well.

We have also performed a comparison of two X16 grids (G6B3X16 and G6B3X16L4) based on the full-physics tropical cyclone test. The final results at day 10 are consistent (see Section 5.2), although two cyclones experience different mesh sizes during the movement. In general, we feel that when one considers to use a mesh with a relatively high densification ratio, having a more gradual and hierarchical way may potentially lead to better quality, but a single-high ratio like X16 is also acceptable. Of course, more practical modeling experience is required. *To avoid ambiguity, we have removed this statement in the revised paper.*

L197: The authors keep referring to grid imprinting in this paragraph. Am I to infer that they are only talking about the spurious waves being generated in the southern hemisphere, in the coarse region of the grid? These features seem to become less noisy when the coarse region increases its resolution, as one would expect. I think it should be stated that the coarser region of G5B3X4 is higher resolution than the coarse region of G6X4.

Reply: Thanks for this comment. Indeed, the imprinting in the southern hemisphere is mainly related to the coarser resolution and mesh irregularities. If one increases the resolution for the coarse part, these imprinting errors can be further reduced (i.e., convergence of the numerical errors can be guaranteed). *We have performed more detailed analysis on the solution errors in the revision (Figures 5-7).* Please see the related paragraphs.

L218: This assertion seems to be mostly true. But I am struck by the oscillations in northern Alaska that are absent in the uniform resolution runs, and which coincide with the mesh transition zone. I think these are real errors. Similar errors are discussed in the context of the SURX4 grid in the following paragraph, but there is no mention of these oscillations in the other VR grids (albeit, they are less noisy than SURX4).

Reply: Indeed, in the initial version, the oscillations in northern Alaska are not reflecting the grid shape, but real errors. They are caused by the increased mesh discontinuity in the VR mode (QU does not support this), and *have been well removed in this version because the hyperdiffusion option is now active.* The flow-dependent Smagorinsky option is inactive over certain regions. *The results now look better.*

L270: Similarly, it looks to me that the vorticity field in 8a is rather oscillatory, especially in the tails of the vortices. I think the authors should investigate whether these are real errors, an artifact of the vorticity calculation, or something else. It would also be interesting to understand the sensitivity of these spurious structures (if they are indeed spurious) to the Smagorinsky coefficient.

Reply: Similar to the last question, *this figure has also been improved due to the hyperdiffusion.* We also compared the results with or without hyperdiffusion (Figure 8). Note that the no-hyperdiffusion case shows more oscillatory solutions than that in the preprint, because the strength of the Smagorinsky diffusion has been reduced for the fine-mesh region in this version (due to the local length scale and a smaller coefficient). *We have added more discussion for this part.*

L288: Can the authors provide the rationale for using different physics-dynamics-tracer coupling methods for hydrostatic vs. non-hydrostatic runs?

Reply: In the initial manuscript, we used DTP split coupling for the nonhydrostatic runs and non-split coupling for the hydrostatic runs simply to confirm that: (i) the nonhydrostatic solver behaves similarly to its hydrostatic counterpart under the hydrostatic regime; (ii) the DTP splitting does not degenerate the model performance when it is properly configured, as compared to a non-split version.

Our previous studies have confirmed these issues in the QU mode, so we hope there is no abnormal behavior in the VR mode as well. Running four combinations would be too much, so we only choose to use the mutually exclusive combinations. As this issue has been validated in the preprint, *only the nonhydrostatic solver with DTP splitting is experimented in the TC test of the revised manuscript.*

L307: "During its movement from the 2nd-refinement into the 1st-refinement region, the change in the grid size leads to little distortion on the tropical cyclone in each experiment." This sentence would be more substantiated if the authors provided a look at how the tropical cyclone fares as it crosses the transition, not just the final structure after it already passed the transition (e.g., Figure 3 in your Zarzycki et al 2013 citation).

Reply: Thanks for this suggestion. *We have provided more details regarding the movement of the tropical cyclone before day 10, in both simple physics and full physics tests.*

L310: The minor disturbance described near where the cyclone was initiated is a common feature of dycores in DCMIP2016. Might be worth looking into whether this result has been published before.

Reply: Thanks for sharing this point. *We have mentioned this in the revised paper.* For this case, the minor disturbance can be suppressed by explicit diffusion. The results of this version almost do not show this because the hyperdiffuion was activated. In the initial version, if we use a higher Smagorinsky coefficient, this minor disturbance can also be suppressed, but hyperdiffusion is more effective. This minor disturbance is not as unrealistic as the new case that we show in the full-physics test, because it is close to the movement path of the major tropical cyclone. Its sensitivity to explicit diffusion is also realistic.

L321: It's unclear to me what the first sentence of this paragraph referencing Ringler has to do with the rest of the paragraph. Could the authors clarify?

Reply: We apologize for your confusion. Here is the reason. For a VR model, the truncation errors are determined by the coarsest part, as Ringlet et al. (2011) and some other studies have pointed out. At a first glance, this seems to be a disadvantage for VR modeling because we cannot reduce the overall truncation errors when the local resolution increases. *As we have further emphasized in the introduction*, the purpose of increasing resolution is to resolve the meteorologically important fine-scale fluid structures. Thus, what we expect from a VR model is that the better resolved fluid structures are not adversely influenced by the greater errors caused by the coarse resolution (and other issues like wave distortion due to mesh transition). Our numerical tests have well supported this point, that is, the local fine-scale structure is more closely related to the fine-resolution, provided that the adverse impacts due to mesh transition and the coarse part can be well controlled. *We have improved this paragraph in the revised manuscript to avoid ambiguity.*

L324: "clone" should say "cyclone."

Reply: Thanks. *This has been corrected.*

L348: More important than what? I'd suggest removing the "more" from the last sentence.

Reply: Thanks. *We have rewritten the entire paragraph.*

Conclusions: I would think that the larger errors found using the SUR generator is a notable conclusion of this paper.

Reply: Thanks. *This statement has been added to the conclusion.*

Figure 4: In the caption "the quasi-uniform G7 and G8 cases" should probably say "G6 and G7 cases," since the l2 norms are defined w.r.t to G8, no?

Reply: The original statement was correct. Computing the top of this shaded area follows Fig. 10 of Jablonowski and Williamson (2006, 10.1256/qj.06.12). It requires using the highest and 2^{nd}-highest resolution tests (G7 and G8 in our case) to compute the uncertainty of the reference solutions.

Configuration and Evaluation of a Global Unstructured Mesh Atmospheric Model (GRIST-A20.9) based on the Variable-Resolution Approach

Yihui Zhou[1,2], Yi Zhang[3], Jian Li[3], Rucong Yu[3], Zhuang Liu[4]

[1]State Key Laboratory of Numerical Modeling for Atmospheric Sciences and Geophysical Fluid Dynamics (LASG), Institute of Atmospheric Physics, Chinese Academy of Sciences, Beijing, China

[2]University of Chinese Academy of Sciences, Beijing, China

[3]State Key Laboratory of Severe Weather (LaSW), Chinese Academy of Meteorological Sciences, China Meteorological Administration, Beijing, China

[4]National Supercomputing Center in Wuxi, Jiangsu, China

***Correspondence to*:** Yi Zhang (yizhang@cma.cn or yizhang@cma.gov.cn)

Abstract. Targeting a long-term effort towards a variable-resolution (VR) global weather and climate model, this study systematically configures and evaluates an unstructured-mesh atmospheric model based on the multiresolution approach. The model performance is examined from dry dynamics to simple and full physics scenarios. In the dry baroclinic wave test, the VR model reproduces comparable fine-scale structures in the refined regions as a fine-resolution quasi-uniform (QU) mesh model. The mesh transition zone does not adversely affect the wave pattern. Regional kinetic energy spectra show that the fine-scale resolving ability improves as the fine resolution increases. Compared to a QU counterpart that has equivalent degrees of freedom, while the VR model tends to increase the global errors, the errors can be reduced when the resolution of the coarse region is increased. The performance over the coarse region is generally close to that of a low-resolution QU counterpart. Two multi-region refinement approaches, the hierarchical and polycentric refinement modes, further validate the model performance under the multiresolution refinement. Activating hyperdiffusion for horizontal velocity is helpful with respect to VR modeling. An idealized tropical cyclone test is further used to examine its ability to resolve fine-scale structures. In the simple physics environment, the VR model can have the tropical cyclone stably pass the transition zone in various configurations. A series of sensitivity tests examines the model performance in a hierarchical refinement mode. The simulations exhibit consistency even when the VR mesh is slightly perturbed by one of the three parameters that control the density function. The tropical cyclone, starting from the 2nd-refinement region and passing through the inner transition zone, gets intensified and covers a smaller area in the refined regions. Such variations are consistent with the behavior that one may observe when uniformly refining the QU mesh. In the full physics environment with a highly variable mesh that reaches sub-10-kilometer resolution, the VR model also produces a reasonable evolution for the tropical cyclone. The explicit diffusion shows its usefulness in terms of suppressing some unrealistic isolated-scale structures that are far away from the initial vortex, and does not adversely affect the physically important object. The fine-scale structure is determined mainly by the fine-resolution area, although the systems may have larger differences before they move into the fine-resolution area. Altogether, this work demonstrates that the multiresolution configuration is a reliable and economic alternative to high-resolution global modeling. The adverse impact due to mesh transition and the coarse region can be well controlled.

1. Introduction

Increasing resolution is generally regarded as an effective way to improve global weather and climate modeling (Jung et al. 2012; Wehner et al. 2014; Zhang et al. 2014; Yu et al. 2019). It is apparent that more computational and storage resources are required for higher resolution models. This leads to a major challenge for efficient model development and application. The emergence of the locally refined, variable-resolution (VR) modeling approach offers a complementary route. The term VR is a broad concept. It may be realized with different styles, such as nested regional modeling with multiple grids, abrupt nonconforming mesh division, stretched grids, and the multiresolution approach. The stretched grid (e.g., Hourdin et al. 2006; Harris et al. 2016) and the multiresolution approaches (e.g., Ringler et al. 2011; Guba et al. 2014) are close in terms of their conforming style. They maintain the global modeling configuration while permitting increased resolution for certain regions. The multiresolution approach is usually realized by an unstructured mesh model, such that a more flexible resolution choice can be achieved by considering multiple regions. Such a global-to-regional approach is the VR style that will be investigated in this study.

Numerical weather and climate modeling has shown that the VR approach can preserve the benefits of high-resolution applications for certain regions at a lower computational cost, as the total number of grid points can be greatly reduced (e.g., Sakaguchi et al. 2015; Skamarock et al. 2018; Gettelman et al. 2018). This advantage is especially valuable for high-resolution modeling that may reach the convection-permitting regime. While the global cloud/storm-resolving (a.k.a., convection-permitting/allowing) modeling approach has been widely adopted (e.g., Stevens et al. 2019), it is still expensive and inefficient to frequently run such models for routine model development, research and application. The VR model provides an efficient testbed for evaluating global model configurations and testing scale-aware physics. It offers flexible resolution configurations that may depend on physical interests. When properly formulated, it can be an intermediate and transitional step before establishing global convection-permitting modeling.

While the VR approach has shown some benefits, it may potentially suffer from some problems[1]. The nonuniform mesh, though it can be gradually refined, hardly decreases the global errors (as compared to its uniform counterpart that has the same degrees of freedom) because the truncation error is controlled mainly by the coarse-resolution region (Weller et al. 2009; Ringler et al. 2011); the numerical convergence rate may also be affected (e.g., Düben and Korn 2014). Mesh refinement also tends to create artificial wave distortion and reflection. This issue is more challenging to the staggered finite-volume methods (Ullrich and Jablonowski 2011), which are widely employed in today's weather and climate models due to their cost-effectiveness. At first glance, this seems to pose some disadvantages. Fortunately, the primary motivation of increasing resolution is to accurately resolve meteorologically important fine-scale structures. This implies that the solutions, in particular at high-wavenumbers, change as the resolution increases. As long as one can maximize the model performance over the refined region, and have good control over the adverse impact due to the non-refined regions, the VR approach based on the staggered finite-volume method is extremely promising. This statement is not intended to diminish the importance of pursuing numerical precision, which is one of several important properties when developing model dynamics. It is hoped that a balanced compromise can be achieved, and thus we can take advantage of this promising approach.

Previous numerical studies have investigated the impact of grid refinement on the solution error in shallow-

[1] We only consider the issues related to model dynamics in this study.

water models (Ringler et al. 2011; Guba et al. 2014), mainly based on single-region refinement. The impact of the width of the grid transition zone and the densification ratio has been emphasized. On the basis of spherical centroid Voronoi tessellation (SCVT), Ringler et al. (2011) demonstrated that the solution error is controlled primarily by the coarse-resolution region, and suggested that this can help to specify the coarse-mesh resolutions by determining what is an acceptable level of accuracy. They also suspected that the width of the transition zone may lead to increased errors. Liu and Yang (2017) suggested that the width of the transition zone may cause smaller additional errors compared to the increase in the densification ratio (for the tests they examined). Within a unified global model, these problems may potentially reduce the performance in the refined region.

In terms of resolving fine-scale fluid structures, the tropical cyclone is a useful testbed, and has been frequently used to examine resolution sensitivity. The global VR approach has been employed to simulate tropical cyclones for cost-effective climate simulations (Zarzycki and Jablonowski 2014). The VR model can capture smoother cloud patterns and smoother mid-level jet structures, leading to enhanced tropical cyclone activities, compared to a nested model in which boundary forcing may have an adverse influence (Hashimoto et al. 2015). Based on the VR mode, the Community Atmosphere Model (CAM) with a spectral element core (Taylor 2011) well maintains tropical cyclones crossing the transition zone without discernable wave reflection (Zarzycki et al. 2014).

While these earlier studies have reported the benefits of VR modeling, a proper utilization of this technique is still challenging and deserves ongoing exploration. In this study, we systematically configure and evaluate the Global-to-Regional Integrated forecast SysTem (GRIST) atmosphere model based on the VR approach. GRIST is a new modeling system developed on an unstructured mesh. Previous studies have described the model formulation, and evaluated its performance in shallow-water model tests (Zhang 2018; Wang et al. 2019), 3D dry dynamical core (dycore[2] hereafter; Zhang et al. 2019; Z19 hereafter) tests, and multiscale moist-atmosphere tests forced by simple physics (Zhang et al. 2020; Z20 hereafter). These studies considered mainly the quasi-uniform (QU) mesh. The model configuration and performance remain underexplored when local mesh refinement is considered.

In this study, we describe the model configuration for VR modeling. In particular, we will detail the explicit diffusion option, and demonstrate its impact. We then examine the model behavior, to understand its strengths and weaknesses under various mesh-refinement styles. This work is intended to provide a basis for utilizing GRIST-VR for more realistic modeling in future. To achieve these goals, we adopt two idealized initial atmospheric conditions, endorsed by the Dynamical Core Model Intercomparison Project (DCMIP; Ullrich et al. 2017). They drive the model towards some well-expected behaviors, facilitating a basic understanding of VR modeling. The model is forced from zero physics (i.e., pure dynamics) to simple and full physics, so as to represent an increasing degree of complexity.

The remainder of this paper is organized as follows. Section 2 presents the model description and its configuration for VR modeling. Section 3 describes the mesh configuration. Section 4 examines the VR performance in the dry baroclinic wave test. Section 5 investigates the model sensitivity in the tropical cyclone test. Section 6 presents a summary.

2. Model description

2.1 Model framework and dynamics

The model evaluated here is a frozen version of the GRIST-Atmosphere model. A20.9 denotes the version

[2] In the context of GRIST, dycore specifically refers to the dry part of the governing equations excluding tracer transport; this should be distinguished from the typical usage of dycore in the literature.

frozen at September 2020. The major description (dynamical framework and component coupling) refers to Z20 and Z19. GRIST is formulated on an unstructured mesh, which permits the use of SCVT (Ringler et al. 2008; Jacobsen et al. 2013) that enables VR modeling. A dry-mass-based generalized vertical coordinate is used. It allows flexible switching between the hydrostatic (HDC) and nonhydrostatic (NDC) cores. The moist-atmospheric model exactly conserves the dry air mass to within machine roundoff. The sink of the moist total energy is limited to a quite small value. The flux-form scalar variables are formulated in a layer-averaged manner. The momentum variables are formulated in their primitive forms. A vertically semi-implicit approach is used for solving the acoustic equations in the NDC, with explicit Eulerian vertical advection. The HDC is fully explicit.

The horizontal discretization is formulated on a hexagonal-C grid, that is, using a kind of staggered finite-volume method. Thuburn et al. (2009) proposed the key construction of the Coriolis term to achieve desirable mimetic properties. Ringler et al. (2010) formulated a set of spatial operators for the nonlinear shallow-water equations, under the constraints of integral invariant conservation and compatible vorticity dynamics. This approach has been used/examined by the Model for Prediction Across Scales (MPAS; Skamarock et al. 2012; Ringler et al. 2013), ICON-IAP (Icosahedral Nonhydrostatic model at the Institute of Atmospheric Physics, Gassmann 2013) and DYNAMICO (Dubos et al. 2015). GRIST adopts two variations that differ from that in Ringler et al. (2010). Zhang (2018) extended a set of high-order upwind/center flux operators (Skamarock and Gassmann 2011) for approximating the edge-based potential vorticity flux, and demonstrated that both the higher nominal order and implicit upwind damping improve the simulated vorticity field. A pure third-order upwind formulation is used in GRIST. The other variation is a redefinition of the kinetic energy term by blending the original primal-cell value with a reconstructed value from the dual cell (Gassmann 2013). This helps to alleviate the noise associated with the Hollingsworth instability (Hollingsworth et al. 1983) according to earlier QU model tests. A default coefficient of 0.9 is used following Eq. (20) in Z19.

The C-grid is cost-effective in dealing with the flux-divergence and gradient operators, which constitute the major horizontal computation involved in a full-fledged atmospheric dynamical core. The potentially adverse dispersion issue due to increasing mesh discontinuity in the VR mode (Ullrich and Jablonowski 2011) can be well controlled by: (i) using a smooth and gradual mesh transition (e.g., SCVT); and (ii) using a slight amount of explicit diffusion (as will be discussed). The basic horizontal operators are nominally accurate to the second-order, while the flux operator can be approximated using higher order extensions. GRIST has several options for the flux operator. Among these, a nominal fifth-order upwind formulation can generate the smallest numerical errors (see results in Zhang 2018; Wang et al. 2019), but is not used for our default configuration as it requires three halo layers (the default number is two)[3]. This formulation is still instrumental in model development, helping to validate that the parallel computing infrastructure (Liu et al. 2020) is working correctly when using different minimum halo layers. The pure upwind formulation of Skamarock and Gassmann (2011) is used for the dycore. When combined with a flux limiter, this scheme can be used for tracer transport (as in Section 5.2). A Two-step Shape-Preserving Advection Scheme (TSPAS; Zhang et al. 2017; Yu 1994) is also a major option for tracer transport (as in Section 5.1). Two-time-level single/multistage forward-in-time integration is used for dycore and tracer transport such that dry air mass and tracer mass are coupled in a consistent manner.

Two initial conditions are used in this study. The baroclinic wave (Jablonowski and Williamson 2006; JW06) examines the adiabatic behaviors in a dry environment. The solution from a high-resolution run can be used as a

[3] Using two halo layers may be possible, but would require a more complicated communication rule than the current one, which is undesirable.

reference solution. The idealized tropical cyclone is initialized following Reed and Jablonowski (2011). It is available from the DCMIP testing scripts. This test does not support a reference solution. As GRIST uses a dry-mass vertical coordinate, obtaining the moist-atmosphere state requires some special treatment (see Z20 for details). All the simulations use 30 full vertical levels with a top at ~2.25 hPa, basically identical to the default CAM5 setup (e.g., Reed and Jablonowski 2012). Both two tests are short-term deterministic tests (i.e., weather forecasting style), helping to validate the model configuration. Long term climate modeling based on the VR configuration will be reported elsewhere. Also note that, while some studies have pointed out that the vertical resolution should increase with horizontal resolution, we keep it unchanged in this study.

2.2 Model physics

The physics–dynamics coupling interface of GRIST is generic and flexible. A tailored package can be used as a plugin, and its development can benefit from the broad community resources. For completeness, we describe them in this section. Three physics packages are currently available for research and development. These packages are separate in the sense that they have different physics drivers and data structures, according to the style of the original host model.

(i) The DCMIP simple physics package. In this study, the scheme of Reed and Jablonowski (2012) is used. It contains a large-scale condensation process, a surface flux scheme, and a boundary layer process. The sea surface temperature is 29℃ globally. These processes are coupled in a time-splitting manner within the package, and the package is coupled to GRIST in a pure operator-splitting approach (ptend_f2_sudden; see Z20).

(ii) A climate physics package adopted from CAM5. This package is not used in this study, but the details can be found in Li et al. (2020). It is currently being tuned for the HDC that targets long-term climate modeling, and can also be used for short-term integration in a weather forecast mode (e.g., Zhang et al. 2015).

(iii) For GRIST-NDC, which is targeted at simulating nonhydrostatic dynamics in a nonhydrostatic regime, a set of parameterization schemes from the Weather Research and Forecast (WRF) model (Powers et al. 2017) has been implemented, and is used in this study. The detailed schemes include: a six-species cloud microphysics scheme (Lin et al. 1983) from WRF version 2.0; the Tiedtke cumulus scheme (Tiedtke 1989) from WRF version 3.7.1; the YSU (Yonsei University) planetary boundary layer scheme (Hong et al. 2006) and a surface scheme from WRF version 2.0; the longwave radiation scheme is the RRTM (Rapid Radiative Transfer Model) from WRF version 2.0 (Mlawer et al. 1997); and the shortwave scheme is a CAM radiation module from WRF version 3.4.1.

The internal coupling of this package is process splitting. All processes start from the dynamics-updated state and send back their respective tendencies to the dynamical model without modifications of the physics state variables. The exception is that microphysics will update the local physics state variables, so the calling sequence still matters. The physics–dynamics coupling uses a hybrid approach that combines the tendency method (ptend_rk) and the operator-splitting approach, as described in Z20. In particular, radiation heating is carried over the internal integration of the dycore as in a tendency method, and other tendencies (microphysics, boundary layer, cumulus) are updated as in a pure operator-splitting approach (ptend_f2_sudden in Z20). We emphasize that this package (including the choice of different schemes and its internal coupling) is still experimental and preliminary. It has not been comprehensively tuned. Ongoing tests and modifications are required to refine the performance. In this study, *it is only intended to evaluate the particular performance of VR modeling and the role of explicit diffusion in a full physics scenario.*

2.3 Time-step choices and explicit diffusion

For a VR model, the time step is theoretically restricted by its fine-resolution region. As emphasized by one reviewer and based on our own experience, some improper VR configurations may lead to higher stability restriction than their equivalent QU counterparts. For example, with regard to the acoustic-mode filter, Klemp et al. (2018) suggested that their original formulation is more problematic in VR applications, and cannot effectively remove the acoustic noise. Uncontrolled acoustic modes may artificially accumulate energy and thus impose a higher stability restriction. For the configurations and tests that we have examined, a suitable configuration of explicit diffusion is mostly relevant to this issue. The details will be given in the following section.

The explicit diffusion tendencies are generated at the largest time interval of each model step (i.e., physics step). They are coupled to model dynamics as in a tendency method (ptend_rk). Z20 showed that the tendency method has a slightly higher stability restriction than the pure operator-splitting approach (ptend_f2_sudden), but it can benefit from the higher accuracy of the time integrator. The tendency method does not require additional data communication. No explicit diffusion is activated for tracer transport in this paper.

2.3.1 Smagorinsky diffusion

Flow-dependent Smagorinsky diffusion (Smagorinsky 1963) is used for velocities and potential temperature, following previous QU model tests. It is activated in all experiments, except the baroclinic wave test at the quasi-uniform G6 resolution. This scheme uses a second-order Laplacian operator multiplied by a flow-dependent eddy viscosity. The eddy viscosity is defined at the edge point. The Smagorinsky diffusion is not very scale selective, but its flow-dependent feature makes it selective in terms of where and how much to diffuse (see e.g., Fig. 9 in Gassmann 2013). The diffusion strength is acceptable overall, as evidenced by the sharp gradient in the QU baroclinic wave test.

In the QU mode, a mean length scale is used for calculating the eddy viscosity. For the VR mode, doing so implies a stronger diffusion (than typically required) for the refinement region. This also leads to a higher stability restriction, especially when the refinement ratio becomes large. In this version, the square of this mean length scale is replaced by the local length product of a pair of crossing edges. In the tropical cyclone test (simple physics), this local approach increases the maximum wind magnitude in the eyewall (as compared to the unscaled version in the preprint), because a smaller amount of diffusion is imposed on the refinement area (see Section 5.1). It also reduces the parametric sensitivity to the Smagorinsky coefficient as found in the preprint. When varying the coefficient, the present version generates more consistent solutions, similar to a QU model. This local scaling approach was used for the VR mode but not for the QU mode.[4]

2.3.2 Hyperdiffusion

The hyperdiffusion option was not used in the initial preprint. Based on some exploration and experiments, we have found that activating scale-selective fourth-order hyperdiffusion for the horizontal velocity shows demonstrable added value for VR modeling. First, in the baroclinic wave test, in the absence of hyperdiffusion, a higher Smagorinsky coefficient (compared to the equivalent QU test) is required to suppress grid-scale noise due to the mesh refinement, which, in turn, restricts the numerical stability. When the hyperdiffusion is activated, we can use a moderate Smagorinsky coefficient that does not challenge the numerical stability, and maintains a quality solution. The DTP (dycore–tracer–physics) splitting mode benefits from this most, because diffusion is called at the step of the model physics. Second, even with a higher coefficient, the Smagorinsky diffusion is inactive over certain regions where weak flow deformation dominates. In the baroclinic wave test, some grid-scale oscillations are more conspicuous over these regions (see preprint). Such noise is due to the mesh transition, and some of it is

---

[4] To achieve consistency with earlier QU tests.

akin to the Hollingsworth instability. As will be shown, activating a background hyperdiffusion for the horizontal wind successfully removes such noise. The solutions are overall less oscillatory than those in the preprint. Third, in the tropical cyclone tests with full physics, which presents more nonlinear feedback, the hyperdiffusion option is also effective in suppressing some isolated-scale structures. Unlike the minor disturbances that may be generated near the major tropical cyclone in the simple physics test, these systems are far away from the initial vortex, and thus highly unrealistic. For these reasons, the hyperdiffusion option is used for the VR mode, but not for the QU test.

The hyperdiffusion operator is formulated by recursively using the Laplacian operator (see Z19 for details). The diffusion coefficient can be determined in a relatively empirical way. For VR modeling, we adopt the approach documented in Zarzycki et al. (2014) for scaling the coefficient:

$$K_4(\Delta x) = K_4(\Delta x^{ref})(\frac{\Delta x}{\Delta x^{ref}})^{3.3219}; \quad (1)$$

The reference length Δx^{ref} and reference viscosity coefficient $K_4(\Delta x^{ref})$ are empirically determined. This formulation reduces $K_4(\Delta x)$ by a factor of 10 for every halving of resolution. A similar scaling approach is also used in MPAS (Skamarock 2016). We typically use the configuration for a G-level resolution that is close to the finest resolution on the mesh. Some typical values for GRIST are documented in Table 1. These values[5] are smaller than those in Zarzycki et al. (2014) for the corresponding length scale by a factor of 5. The local grid distance (Δx) is an average distance between the grid point and all its nearest neighbors, that is, a cell-based value. The edge-based value used for hyperdiffusion is an average of two neighboring cell values.

3. Generation of the VR mesh

The properties and generation of the SCVT are detailed in Ringler et al. (2011) and Ju et al. (2011). We focus on two key elements of the SCVT: generators and density function. A spherical Voronoi tessellation is a spatial subdivision of a sphere Ω based on a set of distinct points on Ω. For each point x_i, $i = 1, \ldots, n$, the corresponding Voronoi region V_i, $i = 1, \ldots, n$, is defined by:

$$V_i = \{x \in \Omega \,\big|\, \|x - x_i\| < \|x - x_j\| \;\; for\ j = 1, \ldots, n\ and\ j \neq i\}; \quad (2)$$

where $\|\cdot\|$ denotes the geodesic distance. Each point x_i is called a generator and its corresponding Voronoi region V_i is called the Voronoi cell. A spherical Voronoi tessellation becomes an SCVT when the generators are also the centroids of the Voronoi cells. In this study, the SCVT mesh is constructed by an iterative process based on Lloyd's algorithm (Du et al. 1999). In particular, a parallel algorithm is used (Jacobsen et al. 2013) to avoid time-consuming serial construction. That said, generating a quality VR SCVT is still nontrivial (but only done once). In our implementation, the iteration stops when two criteria are satisfied: (i) it reaches an empirically determined minimum step; and (ii) the circumcenter of each triangle falls within its shape.

3.1 Generators

Three original generators are used in this study:

(i) **Icosahedron bisection**. This approach benefits from the excellent uniform properties due to bisections of a regular icosahedron. The mesh resolution is referred to as G-level/Gn, where n denotes the number of bisections. After each bisection, the total grid number is approximately four times greater than the previous one.

(ii) **Icosahedron bisection with a final-step trisection**. Instead of using recursive bisection, a trisection is used at the final step, to achieve an intermediate resolution between two neighboring G-level resolutions.

[5] Based on some tests, further halving the coefficient for a given resolution is also acceptable; see Fig. 4.

This mesh is referred to as GnB3 (i.e., n bisections plus one trisection). For instance, the resolution of G5B3 (~80 km) is between that of G6 (~120 km) and that of G7 (~60 km). The number of added primal cells (mainly hexagons) from G5 to G5B3 is equal to four times the number of dual cells (triangles) in G5.

(iii) **Spherical uniform random (SUR) set of points**. Initial points are created uniformly on the sphere by the Monte Carlo method. In this way, the original generators can be obtained by using an arbitrary number of points, not restricted to a sub-divided icosahedron.

3.2 Density function

By specifying the density function, the SCVT is able to precisely control the distribution of the local resolution. For any two Voronoi regions indexed by i and j, the conjecture is:

$$\frac{dx_i}{dx_j} \approx [\frac{\rho(x_j)}{\rho(x_i)}]^{1/4}; \tag{3}$$

where $\rho(x_i)$ is the density function evaluated at x_i, and dx_i measures the local mesh resolution. This relation is valid in a theoretical sense.

A QU mesh can be constructed when the density is one on the sphere, and the Voronoi regions are approximately equivalent to each other. For the VR mesh, the basic density function used in this study is:

$$\rho(x_i) = \frac{1}{2(1-\gamma)}\left[tanh\left(\frac{\beta-\|x_{rc}-x_i\|}{\alpha}\right)+1\right]+\gamma; \tag{4}$$

where $\|x_{rc} - x_i\|$ denotes the geodesic distance between the location of the refinement center and each generator. α indicates the width of the transition zone between the fine-resolution and coarse-resolution regions; β defines the coverage radius of the fine-resolution region; γ measures the densification ratio between the finest and coarsest resolutions. A sample X4 mesh based on this density function with $\gamma = (1/4)^4$ is shown in Fig. 1a.

Because the basic density function is fixed to a single-region refinement, we adjust it for multi-region refinement. The multi-region refinement is divided into two styles based on the refinement centers. In the hierarchical refinement way (Fig. 1b), we add a uniform intermediate-resolution region between the inner fine-resolution and the outer coarse-resolution regions (see Fig. 2). This helps to avoid an overly high densification ratio between two neighboring regions. Eq. (4) can be generalized to a form that allows us to control the resolution of the intermediate region:

$$\rho(x_i) = \frac{1}{2(1-\gamma)}\left[\frac{1-\lambda}{1-\gamma}tanh\left(\frac{\beta_1-\|x_{rc}-x_i\|}{\alpha_1}\right)+\frac{\lambda-\gamma}{1-\gamma}tanh\left(\frac{\beta_2-\|x_{rc}-x_i\|}{\alpha_2}\right)+1\right]+\gamma; \tag{5}$$

λ is designed to control the resolution of the intermediate-resolution region, also referred to as the 2nd-refinement region (dx_{r_2}) that is located between the 1st-refinement (dx_{r_1}) and the coarse-resolution regions (dx_c):

$$\frac{dx_{r_1}}{dx_{r_2}} \approx \lambda^{1/4}; \tag{6}$$

Generally, $\lambda \in [\gamma, 1]$. The function of γ is similar to that in the previous single-region refinement, except that the fine-resolution region is referred to as the 1st-refinement region here:

$$\frac{dx_{r_1}}{dx_c} \approx \gamma^{1/4}; \tag{7}$$

Corresponding to γ, we refer to the meshes that are generated based on λ values of $(1)^4$, $(1/2)^4$, and $(1/3)^4$ as XL1, XL2, and XL3 meshes, since the resolutions of the 1st-refinement and the 2nd-refinement regions vary according to the inner densification ratios of 1, 2, and 3, respectively. For example, when γ is fixed at X4, the hierarchical meshes based on G6 are called G6X4L1, G6X4L2, and G6X4L3 meshes.

In a polycentric refinement mode (Fig. 1c), by adding a different refinement center x_{rc2}, the density function of the polycentric refinement mode is defined as:

$$\rho(x_i) = \frac{1}{2(1-\gamma)}\left[tanh\left(\frac{\beta-\|x_{rc1}-x_i\|}{\alpha}\right) + tanh\left(\frac{\beta-\|x_{rc2}-x_i\|}{\alpha}\right) + 2\right] + \gamma; \quad (8)$$

The geodesic distance between the two refinement centers should satisfy $\|x_{rc1} - x_{rc2}\| > 2\beta$.

4. Dry-atmosphere simulations

4.1 Single-region refinement

The dry-atmosphere test examines the pure numerical solution of the model. It does not include the nonlinear interaction between dynamics, moisture transport, and parameterization. Based on the JW06 baroclinic wave test, we first compare the VR and QU simulations. Previous studies that employed this test for a VR model include Gettelman et al. (2018; using the multiresolution approach) and Harris and Lin (2012; using the multi-grid approach), based on different evaluation metrics. The QU grids include G6 (~120 km; 40962 cells), G7 (~60 km; 163842 cells), and G8 (~30 km; 655362 cells). The VR grids examine all three generators: (i) icosahedral bisection (e.g., G6X4), (ii) final-step trisection (G5B3X4), and (iii) spherical uniform random points (SURX4). The minimum iteration number is 300,000 for G6X4, and 1,000,000 for G5B3X4 and SURX4. The refinement center is placed at 35°N, 180°E, with $\alpha = \pi/20$ and $\beta = \pi/6$. The detailed model configuration is given in Table S1. The timestep of the VR model is limited by its fine-resolution region and is set accordingly, although the currently used timesteps do not represent the maximum allowable step.

We first examine the resolving ability of the fine-scale structures. Figure 4 shows the relative vorticity field at the model level nearest to 850 hPa (level 24) after 10 days. These values have been remapped to the Voronoi cell from the raw triangular grid, so as to avoid the aliasing of certain oscillatory patterns. Such patterns (see preprint) actually reflect the mesh shape, and are more conspicuous for coarse resolution. Figure S1 further shows the QU model results interpolated to the regular longitude–latitude grid as a reference. As the resolution increases, the QU models simulate stronger vortices with a clear filament structure (Fig. 3a–3c). The VR model can simulate the smooth structure of the waves in the refined region, as in the high-resolution QU model. In the VR mode, two vortices in the west fall within the fine-resolution region. The structure of the westernmost vortex in G6X4 (Fig. 3d) is close to G7. G5B3X4 and SURX4 (Fig. 3e, 3f) further produce finer scale structures than G6X4, closer to G8. The easternmost wave falls within the transition zone in three VR runs. The variation in the mesh sizes there does not distort the wave pattern, and the fine-scale structure can be improved as the resolution of the transition zone increases (e.g., from G6X4 to G5B3X4). In the SURX4 test, a minor roughness is found on the tails of the vortices. This deficiency is largely due to local mesh irregularities. Compared to the icosahedron-based SCVT generators, the random generators tend to slightly degrade the mesh quality and the simulation performance.

To present a more quantitative evaluation of the momentum field, we examine regional kinetic energy spectra[6] over the refinement area (red box in Fig. 3). We use the discrete cosine transform to perform this analysis (cf. Denis et al. 2002). The computational procedure is briefly documented in the Appendix. The decomposition is made for relative vorticity and divergence. Fig. 4a–4c show the results from different tests. It is clear that the rotational mode dominates the kinetic energy. The hydrostatic model (Fig. S2) produces similar results to the nonhydrostatic model; thus only the nonhydrostatic core is discussed in the main text.

At the 1st wavenumber, runs with different resolutions show larger discrepancies. This is because this lowest mode absorbs most of the large-scale trend, and corresponds to only a half-cosine wave. Denis et al. (2002) suggested that one may remove this mode if desired, but we keep it here. From the 2nd to the 10th wavenumber,

[6] Note that in Z19, due to an incorrect display setting, there is a plotting mistake in the kinetic energy spectra (their Fig. 9): the tick marks of the entire top *x*-axis (representing wavelength) do not correspond to the actual wavelength of the data. The bottom *x*-axis is correct.

all the curves are consistent overall, suggesting that the well-resolved structures are robust to various tests. The major difference lies in the high wavenumbers. For the VR results, G6X4 is close to G7. This is expected because they have similar resolution over the selected domain (~60 km). For the same reason, G5B3X4 and SURX4 produce better spectral tails than G7 and G6X4, closer to G8. This confirms that increasing the fine resolution of the VR model is able to improve its fine-scale resolving ability. At such high wavenumbers, SURX4 is even closer to G8 as it has slightly higher energy in the tail. However, this actually reflects that SURX4 has slightly more grid-scale oscillations than G5B3X4. Therefore, an examination of kinetic energy spectra should be accompanied by a close look at the real field.

In the context of kinetic energy spectra, it is useful to demonstrate the impact of the hyperviscosity coefficient. On the basis of G5B3X4, we vary the reference hyperviscosity coefficient under a fixed reference length (30 km). Note that 2×10^{12} is the default configuration for this test. As shown in Fig. 4d–4f, when using 2×10^{13}, spectra are seriously damped at the high wavenumbers in both the rotational and divergent components. A flat tail is generated. This indicates that the diffusion strength is overly strong for the fine-resolution area. The other four tests generally produce consistent results: reducing the coefficient tends to slightly uplift the tail, that is, increase the kinetic energy. While the lowest coefficient (2×10^{11}) seems to produce a nicer tail than the default run, this, again, reflects the fact that slightly more small-scale oscillations are generated and the solutions are less clean (but still acceptable). Therefore, when tuning a VR model, one should achieve a minimally required hyperviscosity that neither significantly damps the field nor becomes unable to suppress certain grid-scale oscillations. For this test, 2×10^{12} is fairly close to the optimal choice.

Next, we assess the solution errors by first examining the surface pressure field. Its global distribution on day 9 simulated by GRIST-NDC is shown in Fig. S3. The locations and magnitudes of the high- and low-pressure centers are consistent overall in the QU (Fig. S3a–3c) and VR (Fig. S3d–3f) runs. There are some nonzero wave patterns in all VR simulations over the Southern Hemisphere, reflecting that the nonuniform grid structure leads to higher truncation errors. G5B3X4 has smaller wave patterns than G6X4. This is expected as G5B3X4 has a higher resolution than G6X4 there. Moreover, G5B3X4 is also better than SURX4 with regard to these wave patterns. Considering that SURX4 has more mesh cells, this suggests that generators based on a regular icosahedron produce higher mesh quality than random generators, given roughly the same number of iterations.

Figure 6 shows a quantitative comparison. The global l_2 error norm of each test is computed against the highest resolution (G8). The errors of three VR meshes (G6X4, G5B3X4, and SURX4) are higher overall than those of the QU meshes. Note that these errors are also slightly higher than those in the preprint because a larger time step is used in this version (we performed additional tests to check this sensitivity; figure not shown). The nonhydrostatic solver produces slightly smaller errors using three VR meshes, but the overall accuracy of the two solvers is comparable. For three VR meshes, G5B3X4 shows the smallest error, and is generally close to the results of G6 during the first 10 days. G6X4 shows the largest error and SURX4 lies in between them. Again, the fact that SURX4 is less accurate than G5B3X4 implies that random generators are more likely to be trapped into the local area during the iterative procedure of mesh generation, leading to a higher degree of local irregularity.

For GRIST-NDC, we further tested G7X4 and G8X4. As shown (Fig. 5b), G7X4 produces smaller errors overall than G5B3X4, although the difference is small. G8X4 produces higher errors than G7X4 during the first four days. We suspect this is because certain initial imbalance becomes more active in a high-resolution VR configuration. Such imbalance can be caused by the discrete initialization, for example, the continuous properties imposed by the analytic wind field will not be exactly satisfied by the discrete normal velocity, unless the velocity is obtained based on some constraints. After day 5, G8X4 produces smaller errors than G7X4, and the increment in error reduction is close to the difference between G6X4 and G7X4. G8X4 also produces clearly smaller errors than G6 from day 5 to day 12. After day 13, G8X4 has higher errors than G6, although its coarsest resolution is finer than that of G6. These results suggest that the VR models indeed increase the global errors, but the errors can be reduced by increasing the coarse resolution of the mesh. This is not surprising but a reconfirmation of the conclusion in Ringler et al. (2011), using a 3D atmospheric dynamical core.

The JW06 test was originally proposed in the era that models based on a regular latitude–longitude or Gaussian grid are still popular. For a quasi-uniform grid, it is well known that the steady state in the Southern Hemisphere (or in an unperturbed condition) cannot be perfectly maintained due to mesh irregularity (Lauritzen et al. 2010). In a baroclinic environment, such errors will grow exponentially to break the steady state. Because mesh irregularity increases in a VR mode, the inability to maintain the steady state can be further amplified, ultimately contributing to the increased errors.

To reduce the impact of this issue, we add another perturbation over the Southern Hemisphere to excite two wave trains, as was done in some earlier studies (e.g., Gassmann 2013). Figure 7 shows the relative vorticity field on day 10 from three selected tests: G6, G6X4, and G5B3X4. The sign of the relative vorticity in the Southern Hemisphere is flipped to facilitate a visual comparison. The QU model (Fig. 6a) produces a comparable wave train in each hemisphere. The wave trains are not exactly symmetric because the mesh cells are not exactly symmetric across the equator. In the Northern Hemisphere, G6X4 and G5B3X4 (Fig. 6b and 6c) produce similar solutions to Fig. 3d and 3e. In the Southern Hemisphere, the solution of G5B3X4 is closer to that of G6 than G6X4, in terms of wave pattern and magnitude. This is to be expected as G5B3X4 has higher resolution in the Southern Hemisphere. Although G6X4 cannot simulate the structure in the Southern Hemisphere as G5B3X4, no serious problem is found for that region.

Figure 8 presents a quantitative estimation of the solution error. Generally, the magnitude and the growth of the errors are close to those in Fig. 5b. A notable difference is that G8X4 produces smaller relative errors, closer to those of G7 from day 8 to day 12. On day 15, G8X4 still shows comparable errors to G6. The error reduction from G6X4 to G7X4 also becomes larger than that in Fig. 5b, when the waves become more developed (e.g., day 8 to 11). This implies that the inability to maintain a steady state in the Southern Hemisphere indeed worsens the error estimation for a VR model.

4.2 Multi-region refinement

To increase the application range of the single-region refinement, two multi-region refinement modes are examined to obtain desired resolutions in multiple regions. This represents a unique aspect of the multiresolution approach. The first way is a hierarchical style with one refinement center. It contains three consecutive uniform sub-regions outside the refinement center: the 1st-refinement region, the 2nd-refinement region, and the coarse-resolution region. The 2nd-refinement region provides an intermediate resolution between the 1st-refinement and coarse-resolution regions. Compared to the single-region refinement, this 2nd-refinment region provides more uniform resolution between the refinement center and the coarse-resolution area.

The symmetrical perturbation test was performed using a G8X4L2 mesh. On day 10, the first wave (the strongest) over the Northern Hemisphere is experiencing a higher gradient of resolution than that over the Southern Hemisphere. The fine-scale structures are well captured by the VR model (Fig. 8a). The second and third waves in the Northern Hemisphere have stronger magnitudes than their equivalents in the Southern Hemisphere. The difference in each wave train generally reflects the differences in the local resolution.

The second way uses a polycentric style with multiple refinement centers. The same double-baroclinic wave trains are generated using a G7X4 mesh, with two refinement centers at 35°N, 180°E and 35°S, 180°E, respectively. On day 10, the model well simulates the fine-scale structures over two selected regions (Fig. 8b). The transitions between the fine and coarse regions are smooth and stable. This refinement mode may provide an effective way to simultaneously improve the simulations over different regions. The wave train in the Southern Hemisphere coincides well with that in the North. Again, they are not exactly identical because the mesh cells are not exactly symmetric across the equator.

In this test case, it is useful to demonstrate the impact of activating the hyperdiffusion option. As shown in Fig. 8c and 8d, when hyperdiffusion is turned off, the simulation results become rather oscillatory. The noise pattern at the tail of the wave is akin to the Hollingsworth instability, and is amplified by a VR model due to mesh transition. The noise is more conspicuous in the 1st-refinement region of G8X4L2, due to higher resolution and rapid mesh transition. Also note that these results are more oscillatory than those in the preprint, because the Smagorinsky diffusion in that version is stronger. As mentioned in Section 2.3, even so, the Smagorinsky option is still inactive over certain regions. Using a background hyperdiffusion is a good complement to this deficiency.

5. Moist-atmosphere modeling

5.1 Simple physics

Moist-atmosphere modeling includes the nonlinear interaction of dynamics, moisture transport, and model physics. We use the idealized tropical cyclone test (Reed and Jablonowski 2011) because of its clear resolution sensitivity. This test is useful to examine the VR performance because the solution does not fully converge even at 10 km (Z20). The simulated tropical cyclone is very sensitive to the mesh size. A higher resolution model will produce more intense storms. An initial vortex is placed 10°N, 180°E with no background flow. The tropical cyclone moves northwestward due to beta drift.

Previous studies have shown that model dynamics has a clear impact on the simulations of tropical cyclones. For example, Zhao et al. (2012) showed that increasing the strength of 2D divergence damping in the finite-volume dynamical core (Lin 2004) leads to more occurrences of tropical cyclones. Reed et al. (2015) showed that, in CAM5, the spectral element core produces stronger tropical cyclones than the finite-volume core, when the parameterization suite remains almost unchanged. For GRIST, a known sensitivity is that different tracer transport options may lead to different wind magnitudes in the eyewall, as the full pressure gradient term is, by design, related to tracer mixing ratios (Z20).

We first examine the model behaviors under a simple-physics environment (Reed and Jablonowski 2012). In the preprint, we compared two representative groups of numerical tests: one group based on the NDC with DTP splitting enabled; and one based on the HDC with no DTP splitting (i.e., dycore, tracer transport, and physics use the same time step). Results from these two groups are consistent overall. The impacts of DTP splitting and hydrostatic/nonhydrostatic options do not generate discernable differences across various VR meshes. This is consistent with the previous QU model tests (Z19; Z20) in that: (i) the nonhydrostatic solver behaves similarly to its hydrostatic counterpart under the hydrostatic regime; and (ii) the DTP splitting does not cause a degeneration in performance when it is properly configured. In this version, which uses an updated configuration, only the NDC is tested. The configuration for the simple physics test is given in Table S2.

We first examine the evolution of the tropical cyclone when it moves across the transition zone in the hierarchical refinement mode. The mesh is fixed at X4, with $\alpha_2 = \pi/36$ and $\beta_2 = \pi/4$. In the control run (G6X4L2; Fig. 9a), $\alpha_1 = \pi/36$, $\lambda = (1/2)^4$, and $\beta_1 = \pi/12$. The 1st-refinement region of this VR mesh has

~40-km resolution. Two cases are used to examine the impact of the mesh distribution. In the first case, we choose to use more rapid resolution changes in the inner transition zone based on the two parameters α_1 and λ. α_1 controls the width of the inner transition zone, and λ represents the densification ratio between the 1st- and 2nd-refinement regions. Either narrowing the width of the transition zone (Fig. 9b) or enlarging the inner densification ratio (Fig. 9c) generates a more abrupt transition zone. The other way is to have the transition zone affect the tropical cyclone at an earlier stage. The initial cyclone is placed closer to or even partly within the transition zone by increasing β_1 (Fig. 9d), a parameter that controls the radius of the 1st-refinement region. The tropical cyclone is initialized at 10°N, 180°E over the 2nd-refinement region, near the transition zone between the 1st-refinement and the 2nd-refinement regions.

On day 10, all four tests well simulate the shape of the tropical cyclone. During its movement from the 2nd-refinement into the 1st-refinement region, the change in the grid size leads to little distortion on the tropical cyclone. Compared to the preprint, two major differences can be found. First, the minor disturbances near the major tropical cyclones almost disappear in this version, because activating hyperdiffuion damps the wind field more effectively. Though it can be damped, this minor disturbance is not that unrealistic because it is near the major cyclone. During the movement, it is possible that the nonlinear feedback can generate new small-scale systems. Similar minor disturbances have also been observed in some models participating in DCMIP2016 (see e.g., https://www.earthsystemcog.org/projects/dcmip-2016/). The other difference is that the maximum wind magnitude in the eyewall is stronger overall in this version. This is due to the locally scaled Smagorinsky formulation, as mentioned in Section 2.3.1.

Figure 11 presents the evolution of the tropical cyclone in each test on days 2, 4, 6, and 8. The tropical cyclones in all tests are consistent. No discernable difference is found when they move across the transition. A slightly larger difference is more evident in the early stage (day 2), but such differences diminish as the tropical cyclones move into the refinement center. The relative vorticity field also looks good and does not show any artifacts (Fig. S4). This indicates that the mesh transition does not create notable problems.

To further examine possible sensitivity, we performed a group of experiments by altering one of the three parameters: α_1, β_1, and λ. Figure 12 shows the minimum surface pressure (Fig. 11a–11c) and the maximum wind speed at 850 hPa (Fig. 11e–11f). All these tests use a DTP splitting number 1 : 4 : 8, with a dycore step of 60 s (Table S2). Only one test with the smallest α_1 $(\frac{\pi}{90})$ is unstable at this DTP splitting number, so we adjusted it to 1 : 2 : 4 with the same dycore step. This suggests that an overly narrow inner transition zone can impose a higher stability restriction. The tropical cyclone rapidly strengthens during the first two days. After day 2, it enters into a moderately developing stage in each experiment. The evolution of intensity is diverse. All the VR runs tend to produce stronger tropical cyclones than G6 or G7, because the fine-resolution area determines the ultimate strength. The tests have run-to-run differences, but they are small overall, showing consistent results and robustness.

Figure 13 shows a further comparison between two VR runs (G6X4L2 and G7X4L2) and two QU runs (G7 and G8). The highest resolution of G6X4L2 and G7X4L2 is slightly higher than that of G7 and G8, respectively (see Table S2). As shown, in each comparison (G6X4L2 vs G7, G7X4L2 vs G8), the VR model produces stronger wind magnitudes in the eyewall and a more compact size featuring a smaller area coverage. The eyewall of the cyclone converges towards its center, almost within 1 degree from the center. The maximum winds develop to higher vertical levels as the local resolution increases. Overall, the difference between the VR and QU tests is attributed to different local resolutions.

In the tropical cyclone test, if an unscaled Smagorinsky eddy viscosity is used (Fig. S5; preprint), the VR model will show a higher parametric sensitivity for the Smagorinsky coefficient than the QU model. The current version has largely reduced such sensitivity, closer to the behavior of the QU model (Fig. S5). This confirms the reasonable behavior of the local length formulation.

5.2 Full physics

The simple physics test, while insightful, is limited in the sense that the physics processes are simplified and do not support enough of the nonlinear feedback typical of a real-world model. A VR model may introduce a higher degree of nonlinear feedback due to mesh refinement. Thus, it is useful to check its behavior given a full parameterization suite. We use a more highly variable mesh: G6B3X16L4. The finest part on this mesh reaches ~7–10 km. The refinement center is placed at 35°N, 165°E. The sea surface temperature is identical to that in the simple physics test (29℃ uniformly). The starting date is the first day of June. The solar constant is 1370 $W.m^{-2}$. The DTP splitting number is 1 : 5 : 10 with a dycore step of 10 s. If activated, the square of the Smagorinsky coefficient is 0.005, and the reference hyperviscosity is 2×10^{10} $m^4.s^{-1}$ with a reference length scale of 7000 m.

We first focus on the impact of the explicit diffusion process. Figure 14 shows the tropical cyclones on day 10 from three tests: no explicit diffusion (noDiff), using hyperdiffusion only for the horizontal velocity (hyper), and hyperdiffusion plus Smagorinsky (hyper+smg). The wind speed is shown at the model level nearest to 850 hPa (level 24). On day 10, the tropical cyclone center just moves into the refinement center (35°N, 165°E). In general, the results in the three tests are consistent. The major difference lies in the eyewall. The noDiff and hyper tests produce slightly higher wind maxima than hyper+smg. This suggests that Smagorinsky diffusion becomes active in the eyewall, diffusing the solutions a little bit more strongly. Except for this minor difference (one may need to zoom in to see it), hyper and hyper+smg produce very close solutions.

Explicit diffusion, while it seems to be irrelevant to the performance over the fine-resolution region, plays a more important role in the coarse-resolution region. Due to the globally uniform sea surface temperature, near the South Pole, some isolated systems can be generated in the noDiff test (Fig. 14a). Unlike the possible minor disturbances near the major tropical cyclone in the simple physics test, these systems are not expected there because they are far away from the initial vortex. They are likely to be caused by the nonlinear feedback between dynamics and physics. Only using the Smagorinsky diffusion can suppress them to a certain extent, but not enough due to its flow-dependent nature (Fig. 14b). By further activating the hyperdiffusion option, these systems can be effectively removed (Fig. 14c). This suggests that the explicit diffusion configuration is able to achieve a balance between underdiffusion and overdiffusion.

With this X16 mesh, it is also useful to examine whether a single refinement with a high densification ratio (G6B3X16) tends to create serious problems during the simulation, especially when the tropical cyclone moves across the transition. The refinement center is rotated to 60°N, 165°E. The tropical cyclone will encounter more mesh transitions in G6B3X16. The results are shown in Fig. 15. On day 2, the tropical cyclone in G6B3X16L4 is experiencing mesh cells between ~30 km and ~50 km. In G6B3X16, the encountered mesh sizes are above 70 km. Hence, G6B3X16L4 has a stronger and more developed eyewall at this stage. On day 6, the eyewall enters into a region with cell sizes ~25–30 km in G6B3X16L4, and ~50 km in G6B3X16. G6B3X16L4 still has a more compact eyewall, but the difference between the two runs becomes smaller. On day 10, the eyewalls in both tests enter into an area with cell sizes ~20–25 km. At this stage, both cyclone systems show similar maximum wind magnitudes in the eyewall, and exhibit a similar distribution. Clearly, the fine-scale structure is determined mainly by the fine resolution, although two systems can have larger differences before they enter into the fine-resolution area. These results also demonstrate that a single refinement with a high densification ratio, though more challenging, can perform competitively with a more gradually refined mesh when properly configured (e.g., an overly narrow transition is undesirable). The choice of different mesh styles thus demands more numerical modeling experience and depends on the target issue. This needs to be further examined with the aid of more realistic weather and climate system.

6. Conclusions

In this study, an atmospheric model formulated on an unstructured mesh has been systematically configured and evaluated in its VR mode. Different mesh-refinement styles have been utilized to evaluate the model performance under increasing degrees of complexity, from dry dynamics to simple and then to full physics. Based on some additional NDC tests with full physics, it is found that the QU and VR models (with the same degrees of freedom) have comparable parallel efficiency, that is, the VR configuration does not cause a degeneration in strong scaling performance. This is to be expected as the domain decomposition does not distinguish between QU and VR grids. Other scaling performance (e.g., whether the speedup ratio can achieve the ideal value by simply reducing the total grid number, with all other things being equal) can be found in Liu et al. (2020). Overall, these results demonstrate that the VR configuration of GRIST is a reliable and economic alternative to high-resolution quasi-uniform modeling. The adverse impact due to the mesh transition and the coarse-resolution area can be well controlled. The major conclusions may be summarized in three aspects.

On the overall performance. Based on the dry baroclinic wave test, all VR styles can well capture the fine-scale wave structures. Such fine-scale resolving capability is supported by analysis of regional kinetic energy spectra, and is further verified in the multi-region refinement mode. In the transition zone, the waves are not adversely affected by the mesh refinement. In the coarse-resolution region, the VR model can also simulate an equivalent distribution of waves to its low-resolution counterpart. A VR model indeed produces greater solution errors compared to its QU counterpart that has the same degrees of freedom. However, the solution error can be reduced when the coarse region increases its resolution. Thus, its impact can be controlled. In the tropical cyclone test, the VR model in simple and full physics can simulate the gradual evolution of the tropical cyclone, showing reasonable resolution sensitivity. Importantly, the simulation of the fine-scale structure is controlled mainly by the fine resolution, although larger differences may exist before the systems move into the refinement area. Overall, the adverse impact due to mesh transition and the coarse-mesh region can be well controlled.

On the impact of explicit diffusion. Comparing this version with its earlier version (preprint), the impact of explicit diffusion can be clearly demonstrated. It has been shown that activating scaled hyperdiffuion for the horizontal velocity as background diffusion is helpful in alleviating grid-scale oscillations due to mesh transitions. It also suppresses some highly unrealistic disturbances found in the full physics scenario. When activating hyperdiffuion, it is suggested that a minimally required hyperviscosity should be used, such that it neither significantly damps the field nor becomes unable to suppress undesirable grid-scale disturbances. Using only Smagorinsky diffusion would require higher coefficients to remove oscillations, which, in turn, would restrict the numerical stability. Even so, the Smagorinsky-only configuration is not enough for the VR mode, because it becomes inactive over certain regions that are dominated by weak flow deformation. It is also shown that, in the tropical cyclone test, the scaled Smagorinsky diffusion has much lower parametric sensitivity than its unscaled counterpart. In general, the use of explicit diffusion (properly scaled) plays a positive role in the VR configuration, although there were concerns that their own discretization may introduce additional problems. The increased demands of explicit diffusion from the QU to VR configuration is in accordance with increasing mesh discontinuity due to transitions, and thus should not be viewed as a disadvantage.

On the impact of the mesh styles. Different mesh styles are all able to produce fine-scale structures. They maintain solution quality over the mesh transition and the coarse-resolution area. In the dry test, it has been shown that G5B3X4, while it has fewer cells than SURX4, leads to smaller solution errors and less oscillatory solutions. As these two meshes are generated given a similar number of iterations, this *might* suggest that the random generators need more computation to achieve a quality mesh. In general, when generating a VR mesh, we empirically suggest that one would be better to start from a subdivided icosahedron. In the tropical cyclone case, a series of sensitivity tests examined the model performance in a hierarchical refinement style. The solutions exhibit consistency even when the VR mesh is slightly perturbed by one of the three parameters that control the density function. It is suggested that an overly narrow transition zone should be avoided. In the full physics test, G6B3X16L4 and G6B3X16 produce consistent results on day 10, although the simulations at the initial stage (e.g., day 2) exhibit larger differences.

Code and data availability: GRIST is available at https://github.com/grist-dev. A version of the model code, and running and postprocessing scripts for supporting this paper are available at: https://zenodo.org/record/3930643. Version 2 is for this manuscript, and version 1 is for the preprint. The grid data used to enable the tests are located at https://zenodo.org/record/3817060. Public code access is available after authorization, following https://github.com/GRIST-Dev/TermsAndConditions.

Appendix: Regional kinetic energy spectra analysis

The model data are first interpolated to the Gaussian grid. For the QU model, we use the Gaussian grid that is close to the nominal resolution of the icosahedral mesh (T106 for G6, T213 for G7, and T426 for G8). For the VR model, the data are interpolated based on the fine resolution of the mesh (T221 for G6X4, T328 for G5B3X4, and T328 for SURX4). The selected regional domain (red box in Fig. 3) ranges from 150°E to 150°W and from 30°N to 65°N, with two vortices.

We follow the approach documented by Denis et al. (2002) for computing kinetic energy spectra on a selected regional domain. Let $F_\zeta(m,n)$ be the discrete cosine transform (DCT) of a 2D relative vorticity field $\zeta(i,j)$ of N_i-by-N_j grid points. The variance array can be computed from the DCT field as:

$$\sigma_\zeta^2(m,n) = \frac{F_\zeta^2(m,n)}{N_i N_j}, \tag{A1}$$

where $m = 0, 1, 2, \ldots, N_i - 1$, $n = 0, 1, 2, \ldots, N_j - 1$, and $(m,n) \neq (0,0)$. Each 2D wavenumber pair (m,n) is associated with a wavelength:

$$A = \frac{2\Delta}{\mu}, \tag{A2}$$

where Δ is the grid spacing. μ is a normalized 2D wavenumber defined as:

$$\mu = \sqrt{\frac{m^2}{N_i^2} + \frac{n^2}{N_j^2}}. \tag{A3}$$

To construct a spectrum, the variance contributions of $F_\zeta(m,n)$ needs to be binned by bands of μ. The ranges of μ for a given wavelength band are determined as follows:

$$\mu(k) = \frac{k}{\min(N_i, N_j)}, \tag{A4}$$

$$\mu(k) + \Delta\mu(k) = \frac{k+1}{\min(N_i, N_j)}, \tag{A5}$$

where $k = 1, 2, 3, \ldots, \min(N_i, N_j) - 1$ denotes the wavenumber.

The rotational part of a spectrum as a function of wavenumber k can be obtained by binning each element in the variance array. For a given k, Eqs. (A4) and (A5) are used to calculate the lower and upper bounds. For each variance element, if the corresponding μ satisfies $\mu(k) < \mu < \mu(k) + \Delta\mu(k)$, the variance will be summed to give the spectrum for this k, that is:

$$E_\zeta(k) = \frac{1}{2}\sum_{\mu(k)}^{\mu(k)+\Delta\mu(k)} \frac{\sigma_\zeta^2(m,n)}{\hat{k}^2}, \tag{A6}$$

where $\hat{k}$ is the circular wavenumber:

$$\hat{k} = \frac{\pi}{\Delta}\mu. \tag{A7}$$

Similarly, the divergent part can be evaluated based on the divergence field:

$$E_D(k) = \frac{1}{2}\sum_{\mu(k)}^{\mu(k)+\Delta\mu(k)} \frac{\sigma_D^2(m,n)}{\hat{k}^2}, \tag{A8}$$

where $\sigma_D^2(m,n)$ is the variance array of divergence. The total kinetic energy as a function of wavenumber k is given as:

$$E(k) = E_\zeta(k) + E_D(k), \tag{A9}$$

In this study, kinetic energy spectra are displayed as a function of wavelength A and wavenumber k. It should be noted that the lowest mode ($k = 1$) absorbs most of the large-scale trend and can be excluded if needed (cf. Denis et al. 2002).

Supplement: vr_supplement.pdf contains Table S1, S2 and Figures S1–S5.

Author contribution: Y. Zhou performed the mesh generation, most data analysis, and an initial exploration of VR modeling, with input and guidance from Y. Zhang. R. Yu supervised Y. Zhou's work, provided impetus and resources, guided experimental design. J. Li supervised the project of model development. Z. Liu is responsible for parallel computing, and customized the parallel mesh generation software. Y. Zhang designed this study, developed and maintained the model, performed production runs, and analyzed the simulations. Y. Zhang and Y. Zhou wrote the manuscript, with contributions from all authors. All the authors continuously discussed the model development.

Competing interests. The authors declare that they have no conflict of interest.

Acknowledgments. The constructive comments from two anonymous reviewers are highly appreciated. This study was supported by the National Natural Science Foundation of China (41875135; 41675075), the National Key R&D Program of China (2017YFC1502202; 2016YFA0602101), and the S&T Development Fund of CAMS (2019KJ011).

References

Denis, B., J. Côté, and R. Laprise, 2002: Spectral Decomposition of Two-Dimensional Atmospheric Fields on Limited-Area Domains Using the Discrete Cosine Transform (DCT). *Monthly Weather Review*, **130,** 1812-1829.

Du, Q., V. Faber, and M. Gunzburger, 1999: Centroidal Voronoi tessellations: Applications and algorithms. *Siam Review*, **41,** 637-676.

Düben, P. D., and P. Korn, 2014: Atmosphere and Ocean Modeling on Grids of Variable Resolution—A 2D Case Study. *Monthly Weather Review*, **142,** 1997-2017.

Dubos, T., S. Dubey, M. Tort, R. Mittal, Y. Meurdesoif, and F. Hourdin, 2015: DYNAMICO-1.0, an icosahedral hydrostatic dynamical core designed for consistency and versatility. *Geosci. Model Dev.*, **8,** 3131-3150.

Gassmann, A., 2013: A global hexagonal C-grid non-hydrostatic dynamical core (ICON-IAP) designed for energetic consistency. *Quarterly Journal of the Royal Meteorological Society*, **139,** 152-175.

Gettelman, A., and Coauthors, 2018: Regional Climate Simulations With the Community Earth System Model.

Journal of Advances in Modeling Earth Systems, **10,** 1245-1265.

Guba, O., M. A. Taylor, P. A. Ullrich, J. R. Overfelt, and M. N. Levy, 2014: The spectral element method (SEM) on variable-resolution grids: evaluating grid sensitivity and resolution-aware numerical viscosity. *Geoscientific Model Development*, **7,** 2803-2816.

Harris, L. M., and S.-J. Lin, 2012: A Two-Way Nested Global-Regional Dynamical Core on the Cubed-Sphere Grid. *Monthly Weather Review*, **141,** 283-306.

Harris, L. M., S.-J. Lin, and C. Tu, 2016: High-Resolution Climate Simulations Using GFDL HiRAM with a Stretched Global Grid. *Journal of Climate*, **29,** 4293-4314.

Hashimoto, A., J. M. Done, L. D. Fowler, and C. L. Bruyère, 2015: Tropical cyclone activity in nested regional and global grid-refined simulations. *Climate Dynamics*, **47,** 497-508.

Hollingsworth, A., P. Kållberg, V. Renner, and D. M. Burridge, 1983: An internal symmetric computational instability. *Quarterly Journal of the Royal Meteorological Society*, **109,** 417-428.

Hong, S.-Y., Y. Noh, and J. Dudhia, 2006: A New Vertical Diffusion Package with an Explicit Treatment of Entrainment Processes. *Monthly Weather Review*, **134,** 2318-2341.

Hourdin, F., and Coauthors, 2006: The LMDZ4 general circulation model: climate performance and sensitivity to parametrized physics with emphasis on tropical convection. *Climate Dynamics*, **27,** 787-813.

Jablonowski, C., and D. L. Williamson, 2006: A baroclinic instability test case for atmospheric model dynamical cores. *Quart. J. Roy. Meteor. Soc.*, **132,** 2943-2975.

Jacobsen, D. W., M. Gunzburger, T. Ringler, J. Burkardt, and J. Peterson, 2013: Parallel algorithms for planar and spherical Delaunay construction with an application to centroidal Voronoi tessellations. *Geoscientific Model Development*, **6,** 1353-1365.

Ju, L., T. Ringler, and M. Gunzburger, 2011: Voronoi tessellations and their application to climate and global modeling. *Numerical Techniques for Global Atmospheric Models, P. H. Lauritzen et al., Eds. Lecture Notes in Computational Science and Engineering*, **80, Springer-Verlag,** 313-342.

Jung, T., and Coauthors, 2012: High-Resolution Global Climate Simulations with the ECMWF Model in Project Athena: Experimental Design, Model Climate, and Seasonal Forecast Skill. *Journal of Climate*, **25,** 3155-3172.

Klemp, J. B., W. C. Skamarock, and S. Ha, 2018: Damping Acoustic Modes in Compressible Horizontally Explicit Vertically Implicit (HEVI) and Split-Explicit Time Integration Schemes. *Monthly Weather Review*, **146,** 1911-1923.

Lauritzen, P. H., C. Jablonowski, M. A. Taylor, and R. D. Nair, 2010: Rotated Versions of the Jablonowski Steady-State and Baroclinic Wave Test Cases: A Dynamical Core Intercomparison. *Journal of Advances in Modeling Earth Systems*, **2,** 15.

Li, X., Y. Zhang, X. Peng, and J. Li, 2020: Using a single column model (SGRIST 1.0) for connecting model physics and dynamics in a global-to-regional integrated forecast system. *Manuscript submitted to GMD*.

Lin, S.-J., 2004: A "Vertically Lagrangian" Finite-Volume Dynamical Core for Global Models. *Monthly Weather Review*, **132,** 2293-2307.

Lin, Y.-L., R. D. Farley, and H. D. Orville, 1983: Bulk Parameterization of the Snow Field in a Cloud Model. *Journal of Climate and Applied Meteorology*, **22,** 1065-1092.

Liu, Y., and T. Yang, 2017: Impact of Local Grid Refinements of Spherical Centroidal Voronoi Tessellations for Global Atmospheric Models. *Communications in Computational Physics*, **21,** 1310-1324.

Liu, Z., Y. Zhang, X. Huang, J. Li, D. Wang, M. Wang, and X. Huang, 2020: Development and performance optimization of a parallel computing infrastructure for an unstructured-mesh modelling framework. *Geosci. Model Dev. Discuss.*, **2020,** 1-32.

Mlawer, E. J., S. J. Taubman, P. D. Brown, M. J. Iacono, and S. A. Clough, 1997: Radiative transfer for inhomogeneous atmospheres: RRTM, a validated correlated-k model for the longwave. *J. Geophys. Res.*, **102,** 16663-16682.

Powers, J. G., and Coauthors, 2017: The Weather Research and Forecasting Model: Overview, System Efforts, and Future Directions. *Bulletin of the American Meteorological Society*, **98,** 1717-1737.

Reed, K. A., and C. Jablonowski, 2011: An Analytic Vortex Initialization Technique for Idealized Tropical Cyclone Studies in AGCMs. *Monthly Weather Review*, **139,** 689-710.

——, 2012: Idealized tropical cyclone simulations of intermediate complexity: A test case for AGCMs. *Journal of Advances in Modeling Earth Systems*, **4**.

Reed, K. A., and Coauthors, 2015: Impact of the dynamical core on the direct simulation of tropical cyclones in a high-resolution global model. *Geophysical Research Letters*, **42,** 3603-3608.

Ringler, T., L. Ju, and M. Gunzburger, 2008: A multiresolution method for climate system modeling: application of spherical centroidal Voronoi tessellations. *Ocean Dynamics*, **58,** 475-498.

Ringler, T., M. Petersen, R. L. Higdon, D. Jacobsen, P. W. Jones, and M. Maltrud, 2013: A multi-resolution approach to global ocean modeling. *Ocean Modelling*, **69,** 211-232.

Ringler, T. D., J. Thuburn, J. B. Klemp, and W. C. Skamarock, 2010: A unified approach to energy conservation and potential vorticity dynamics for arbitrarily-structured C-grids. *Journal of Computational Physics*, **229,** 3065-3090.

Ringler, T. D., D. Jacobsen, M. Gunzburger, L. Ju, M. Duda, and W. Skamarock, 2011: Exploring a Multiresolution Modeling Approach within the Shallow-Water Equations. *Monthly Weather Review*, **139,** 3348-3368.

Sakaguchi, K., and Coauthors, 2015: Exploring a Multiresolution Approach Using AMIP Simulations. *Journal of Climate*, **28,** 5549-5574.

Skamarock, W., 2016: NGGPS/DTG briefing on MPAS configuration options. *http://www2.mmm.ucar.edu/people/skamarock/Presentations/MPAS_config_overview_20160122.pdf*.

Skamarock, W. C., and A. Gassmann, 2011: Conservative Transport Schemes for Spherical Geodesic Grids: High-Order Flux Operators for ODE-Based Time Integration. *Monthly Weather Review*, **139,** 2962-2975.

Skamarock, W. C., J. B. Klemp, M. G. Duda, L. D. Fowler, S.-H. Park, and T. D. Ringler, 2012: A Multiscale Nonhydrostatic Atmospheric Model Using Centroidal Voronoi Tesselations and C-Grid Staggering. *Monthly Weather Review*, **140,** 3090-3105.

Skamarock, W. C., M. G. Duda, S. Ha, and S.-H. Park, 2018: Limited-Area Atmospheric Modeling Using an Unstructured Mesh. *Monthly Weather Review*, **146,** 3445-3460.

Smagorinsky, J., 1963: GENERAL CIRCULATION EXPERIMENTS WITH THE PRIMITIVE EQUATIONS. *Monthly Weather Review*, **91,** 99-164.

Stevens, B., and Coauthors, 2019: DYAMOND: the DYnamics of the Atmospheric general circulation Modeled On Non-hydrostatic Domains. *Progress in Earth and Planetary Science*, **6,** 61.

Taylor, M. A., 2011: Conservation of Mass and Energy for the Moist Atmospheric Primitive Equations on Unstructured Grids. *Numerical Techniques for Global Atmospheric Models*, P. Lauritzen, C. Jablonowski, M. Taylor, and R. Nair, Eds., Springer Berlin Heidelberg, 357-380.

Thuburn, J., T. D. Ringler, W. C. Skamarock, and J. B. Klemp, 2009: Numerical representation of geostrophic modes on arbitrarily structured C-grids. *Journal of Computational Physics*, **228,** 8321-8335.

Tiedtke, M., 1989: A Comprehensive Mass Flux Scheme for Cumulus Parameterization in Large-Scale Models. *Monthly Weather Review*, **117,** 1779-1800.

Ullrich, P. A., and C. Jablonowski, 2011: An analysis of 1D finite-volume methods for geophysical problems on refined grids. *Journal of Computational Physics*, **230,** 706-725.

Ullrich, P. A., and Coauthors, 2017: DCMIP2016: a review of non-hydrostatic dynamical core design and intercomparison of participating models. *Geosci. Model Dev.*, **10,** 4477-4509.

Wang, L., Y. Zhang, J. Li, Z. Liu, and Y. Zhou, 2019: Understanding the Performance of an Unstructured-Mesh Global Shallow Water Model on Kinetic Energy Spectra and Nonlinear Vorticity Dynamics. *Journal of Meteorological Research*, **33,** 1075-1097.

Wehner, M. F., and Coauthors, 2014: The effect of horizontal resolution on simulation quality in the Community Atmospheric Model, CAM5.1. *Journal of Advances in Modeling Earth Systems*, **6,** 980-997.

Weller, H., H. G. Weller, and A. Fournier, 2009: Voronoi, Delaunay, and Block-Structured Mesh Refinement for Solution of the Shallow-Water Equations on the Sphere. *Monthly Weather Review*, **137,** 4208-4224.

Yu, R., 1994: A Two-Step Shape-Preserving Advection Scheme. *Adv. Atmos. Sci.*, **11(4),** 479-490.

Yu, R., Y. Zhang, J. Wang, J. Li, H. Chen, J. Gong, and J. Chen, 2019: Recent Progress in Numerical Atmospheric Modeling in China. *Advances in Atmospheric Sciences*, **36,** 938-960.

Zarzycki, C. M., and C. Jablonowski, 2014: A multidecadal simulation of Atlantic tropical cyclones using a variable-resolution global atmospheric general circulation model. *Journal of Advances in Modeling Earth Systems*, **6,** 805-828.

Zarzycki, C. M., C. Jablonowski, and M. A. Taylor, 2014: Using Variable-Resolution Meshes to Model Tropical Cyclones in the Community Atmosphere Model. *Monthly Weather Review*, **142,** 1221-1239.

Zhang, Y., H. Chen, and R. Yu, 2014: Simulations of Stratus Clouds over Eastern China in CAM5: Sensitivity to Horizontal Resolution. *Journal of Climate*, **27,** 7033-7052.

——, 2015: Simulations of Stratus Clouds over Eastern China in CAM5: Sources of Errors. *Journal of Climate*, **28,** 36-55.

Zhang, Y., R. Yu, and J. Li, 2017: Implementation of a conservative two-step shape-preserving advection scheme on a spherical icosahedral hexagonal geodesic grid. *Adv. Atmos. Sci.*, **34,** 411-427.

Zhang, Y., 2018: Extending High-Order Flux Operators on Spherical Icosahedral Grids and Their Applications in the Framework of a Shallow Water Model. *Journal of Advances in Modeling Earth Systems*, **10,** 145-164.

Zhang, Y., J. Li, R. Yu, S. Zhang, Z. Liu, J. Huang, and Y. Zhou, 2019: A Layer-Averaged Nonhydrostatic Dynamical Framework on an Unstructured Mesh for Global and Regional Atmospheric Modeling: Model Description, Baseline Evaluation, and Sensitivity Exploration. *Journal of Advances in Modeling Earth Systems*, **11,** 1685-1714.

Zhang, Y., J. Li, R. Yu, Z. Liu, Y. Zhou, X. Li, and X. Huang, 2020: A Multiscale Dynamical Model in a Dry-mass Coordinate for Weather and Climate Modeling: Moist Dynamics and its Coupling to Physics. *Monthly Weather Review*.

Zhao, M., I. M. Held, and S.-J. Lin, 2012: Some Counterintuitive Dependencies of Tropical Cyclone Frequency on Parameters in a GCM. *Journal of the Atmospheric Sciences*, **69,** 2272-2283.

Table 1 A list of typical values of reference length and hyperviscosity coefficient.

Reference length (m)	Reference hyperviscosity coefficient ($m^4.s^{-1}$)
120 000	2e14
60 000	2e13
40 000	8e12
30 000	2e12
15 000	2e11
7 500	2e10

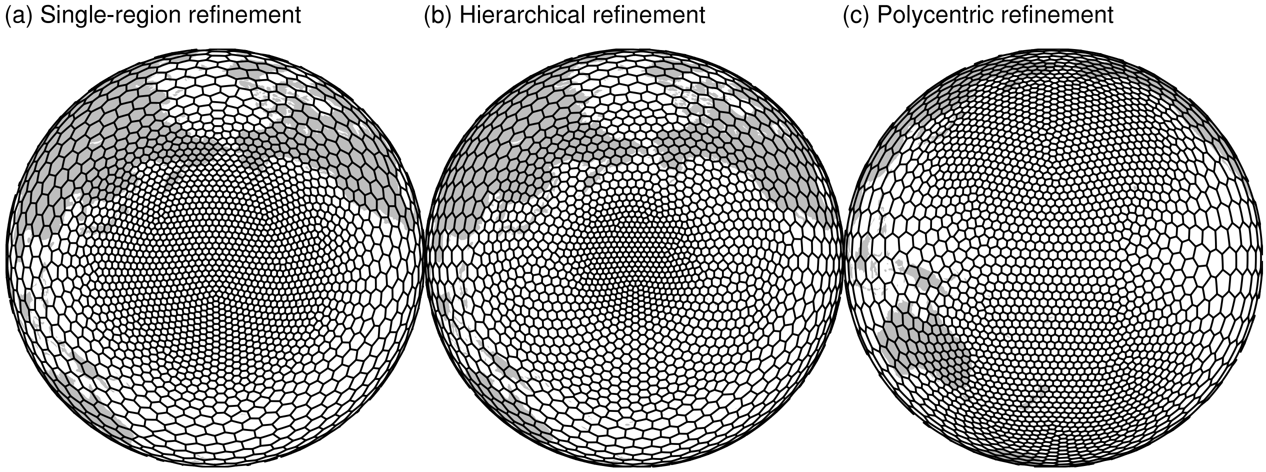

Figure 2: An illustration of the variable-resolution mesh (X4) based on three density functions: (a) single-region refinement, (b) hierarchical refinement, and (c) polycentric refinement.

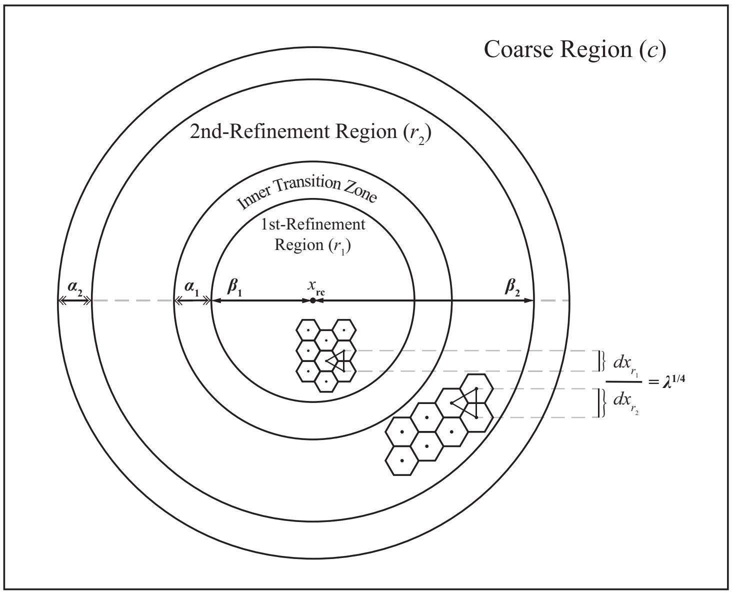

Figure 3: A schematic diagram of the hierarchical refinement mesh, illustrating the function of three parameters of the density function. α_1 and α_2 control the width of the transition zones; λ represents the inner densification ratio between the 1^{st}-refinement and 2^{nd}-refinement resolution regions; β_1 and β_2 control the coverage radius of the 1^{st}-refinement and 2^{nd}-refinement regions.

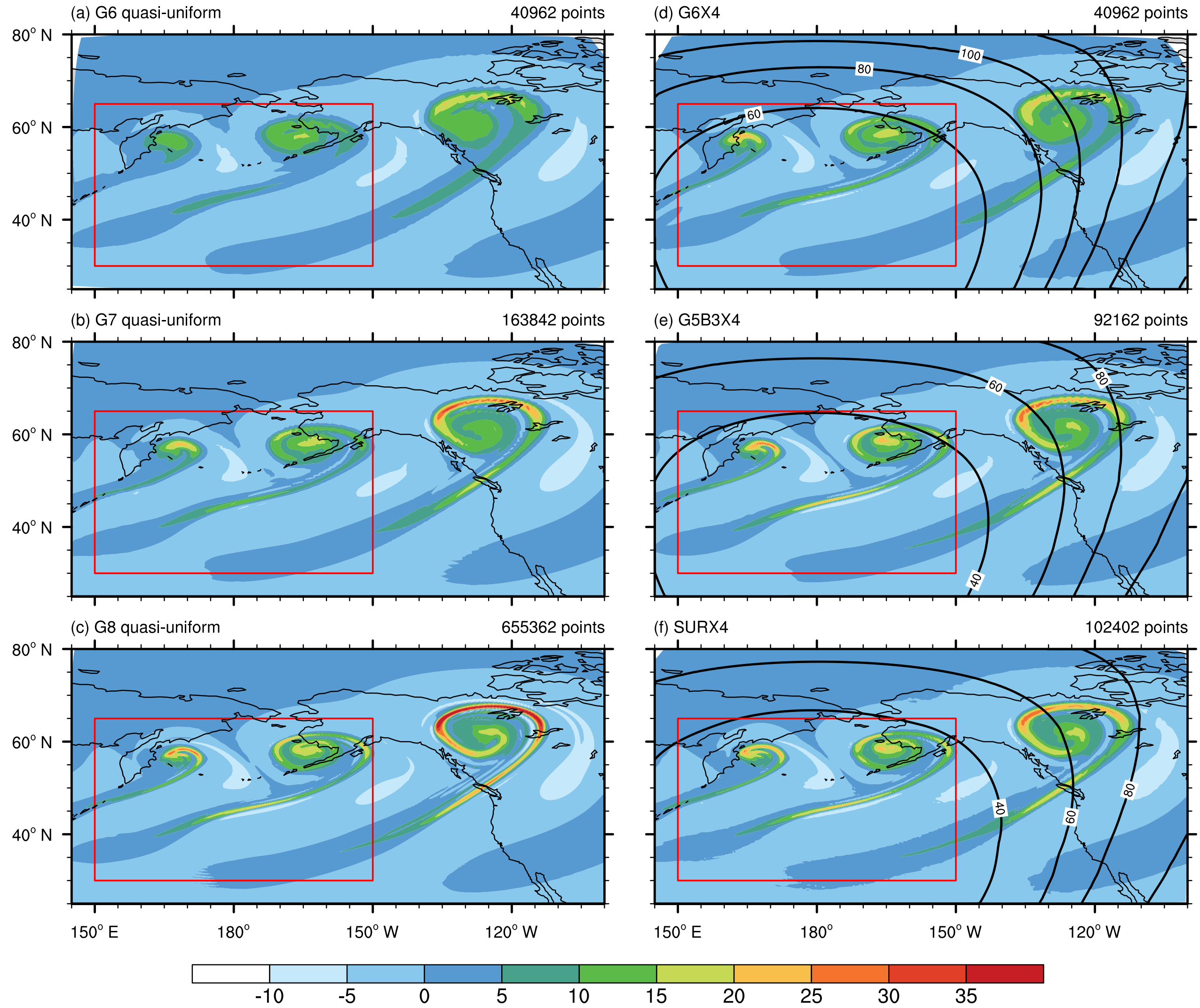

Figure 4: The relative vorticity (10^{-5} s^{-1}) field at the model level nearest to 850 hPa (level 24) after 10 days. The quasi-uniform (left-hand column) and variable-resolution (right-hand column) results are shown. The contour lines denote the mesh resolution (km). The vorticity is remapped from the raw triangular cell to the Voronoi cell using an area-weighted approach (true for all vorticity values shown in this study). Also see Figure S2 for the remapped QU-model solutions on a regular latitude–longitude grid. The red box denotes the region for regional kinetic energy analysis in Fig. 4. The contour lines denote the smoothed mesh cell sizes (km).

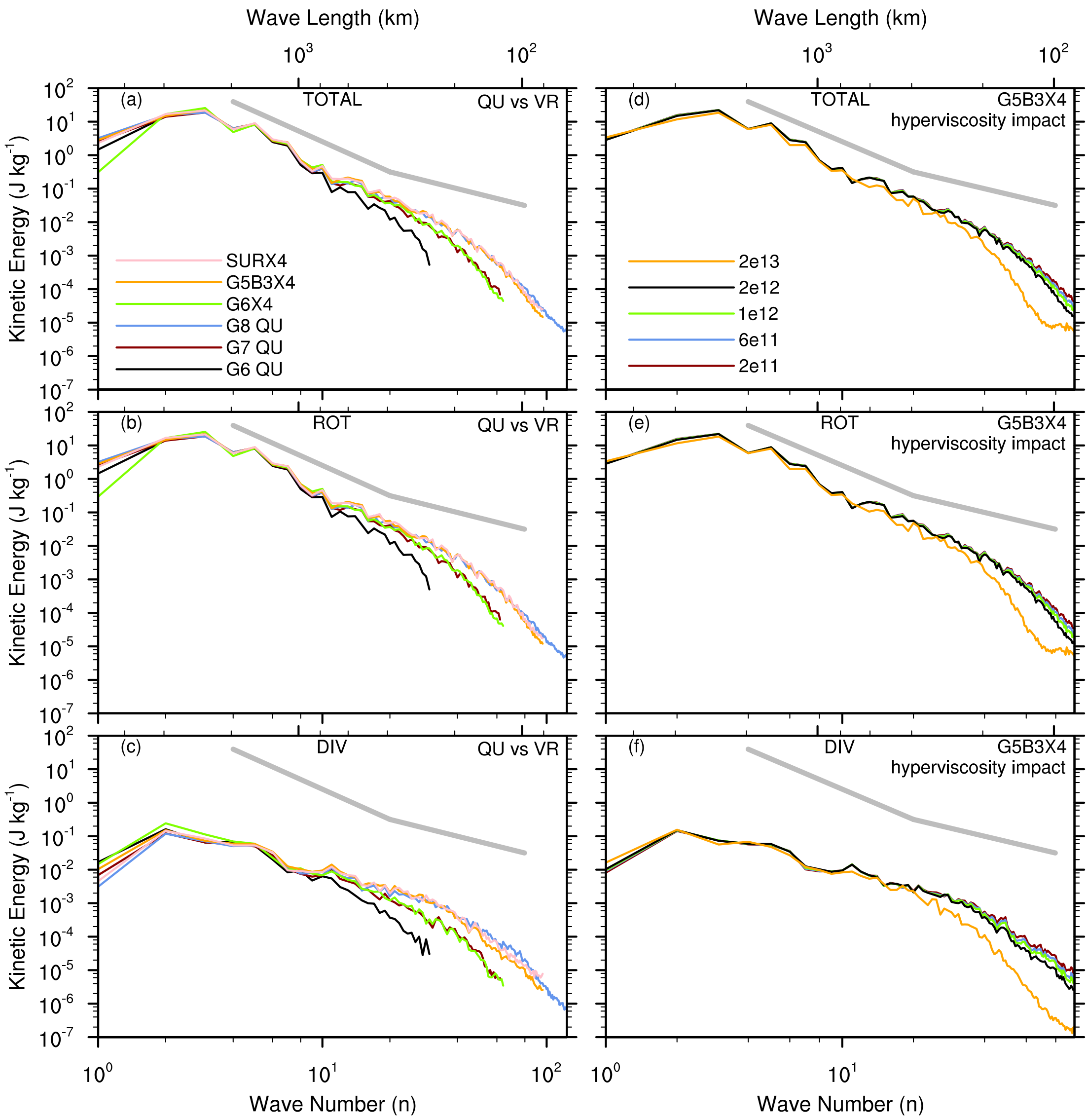

Figure 5: Baroclinic wave: horizontal regional kinetic energy spectra (unit: J kg^{-1}) at the model level nearest to 850 hPa on day 10, (a) total kinetic energy, (b) the rotational component, and (c) the divergence component. The results of the nonhydrostatic core are shown here, while the results for the hydrostatic core can be found in Fig. S2. The right-hand column (d)–(f) examines the impact of varying the hyperviscosity coefficient on spectra. The thick gray lines denote the -3 and $-5/3$ slopes, respectively.

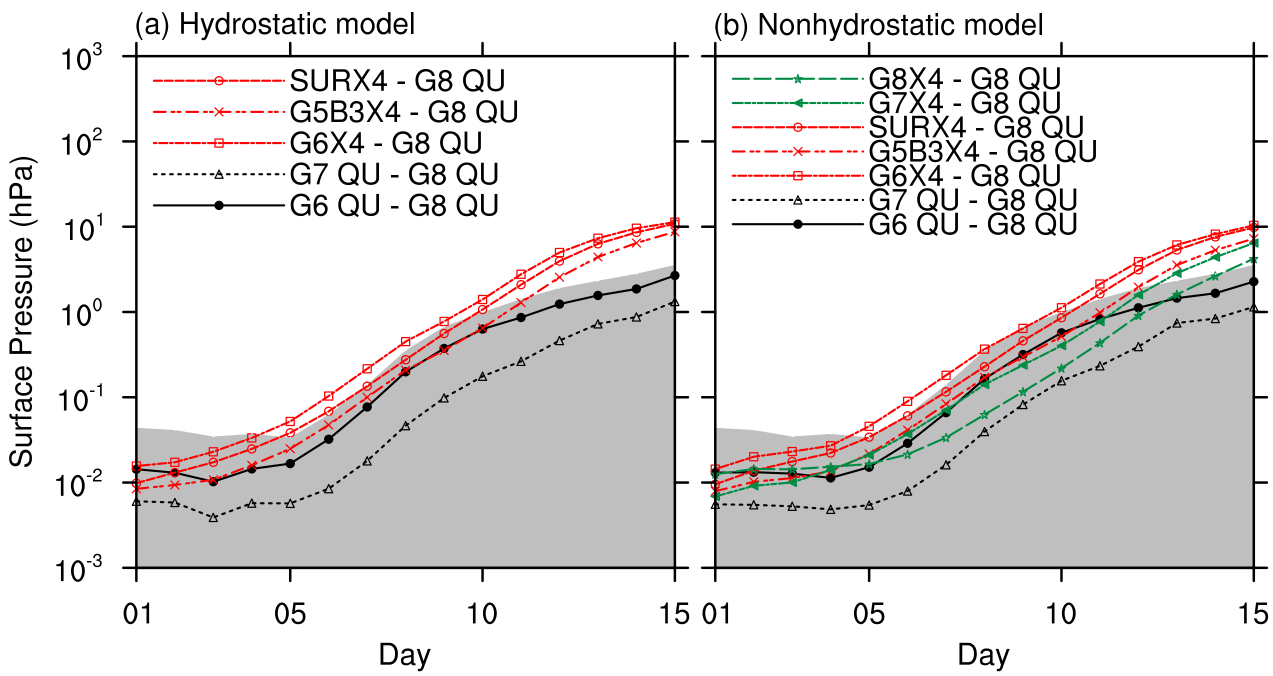

Figure 6: Baroclinic wave test: the l_2 error norms of surface pressure as a function of time for (a) the hydrostatic and (b) the nonhydrostatic dynamical core. The error is computed against the high-resolution quasi-uniform G8 mesh. The gray area denotes the uncertainty in the reference solutions, which selects the maximum l_2 error norms from four curves (HDC and NDC at G7 and G8 as four cases). Details can be found in Jablonowski and Williamson (2006).

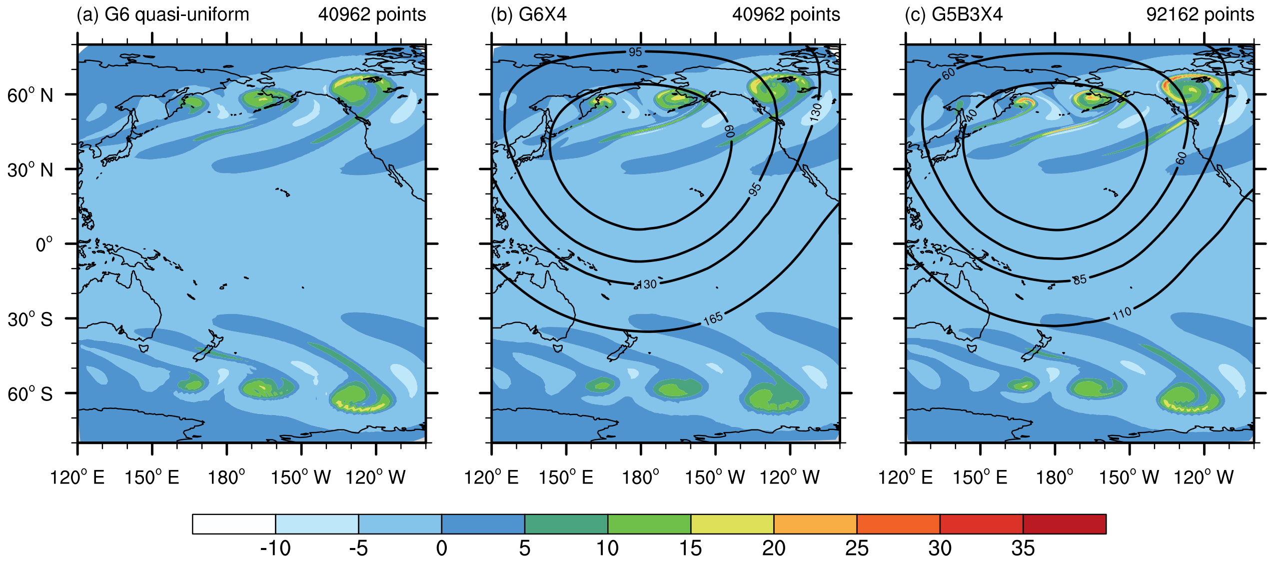

Figure 7: Adding a symmetrical perturbation in the Southern Hemisphere in the baroclinic wave test. The relative vorticity (10^{-5} s^{-1}) field at the model level nearest to 850 hPa on day 10 is shown for (a) quasi-uniform G6, (b) variable-resolution G6X4, and (c) G5B3X4 meshes. Only the nonhydrostatic core is used. The values in the Southern Hemisphere are substituted by their opposite values. The raw vorticity values on the triangular cell have been remapped to the Voronoi cell. The contour lines denote the smoothed mesh cell sizes (km).

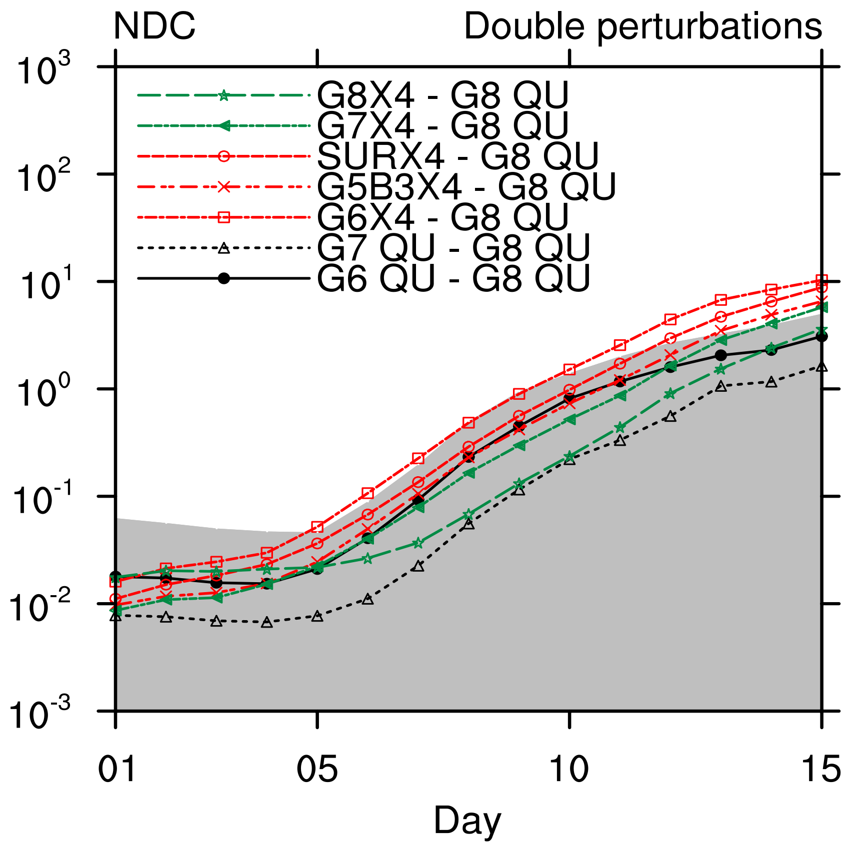

Figure 8 Same as Fig. 5, but for the baroclinic wave test with double perturbations, only for the nonhydrostatic core.

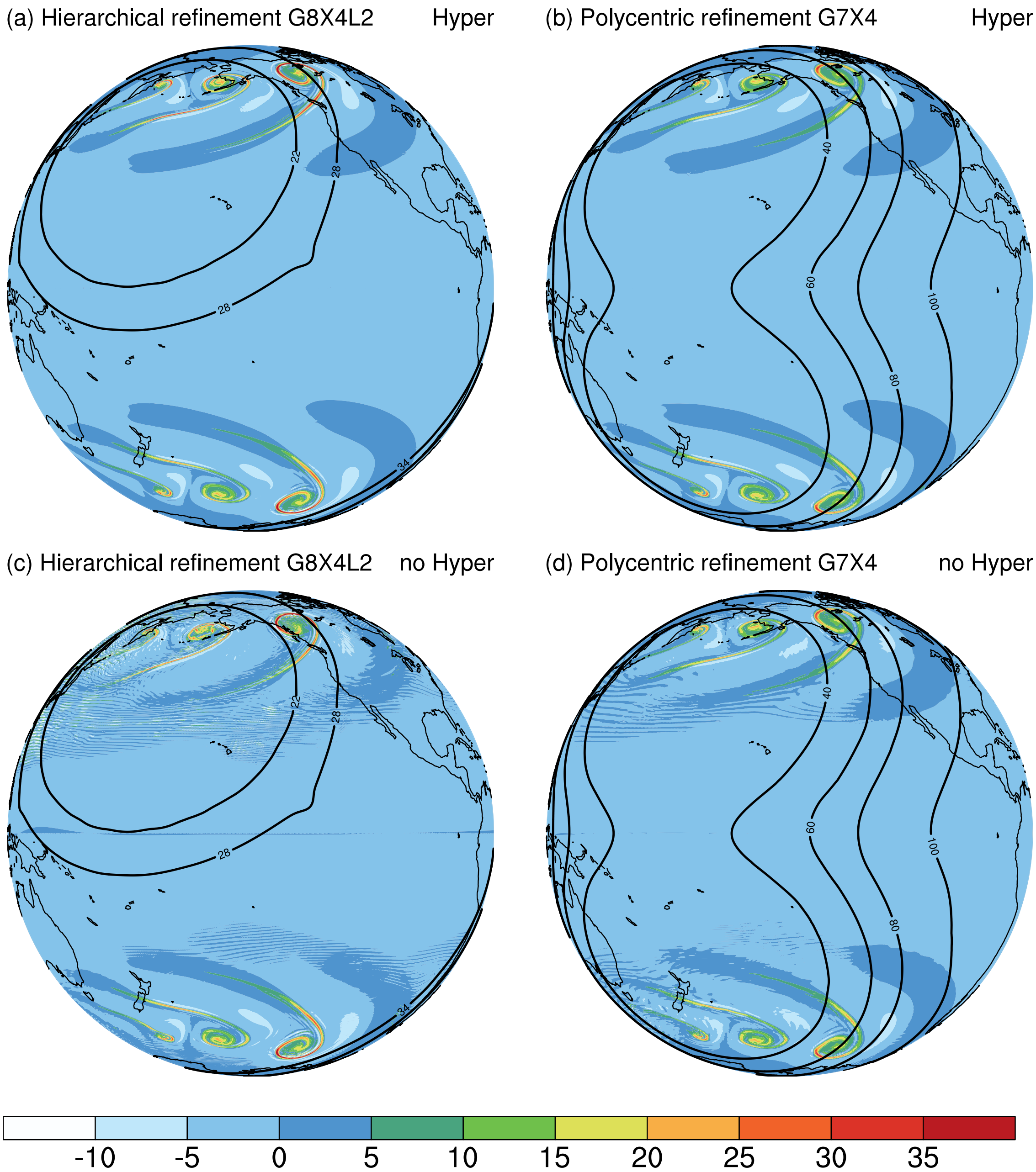

Figure 9: As in Fig. 6, but for two multi-region refinement meshes: (a) a hierarchical refinement style (G8X4L2) and (b) a polycentric refinement mesh based on G7X4. (c) (d) same as (a) (b), but for runs that turn off the hyperdiffusion option. The contour lines denote the smoothed mesh cell sizes (km).

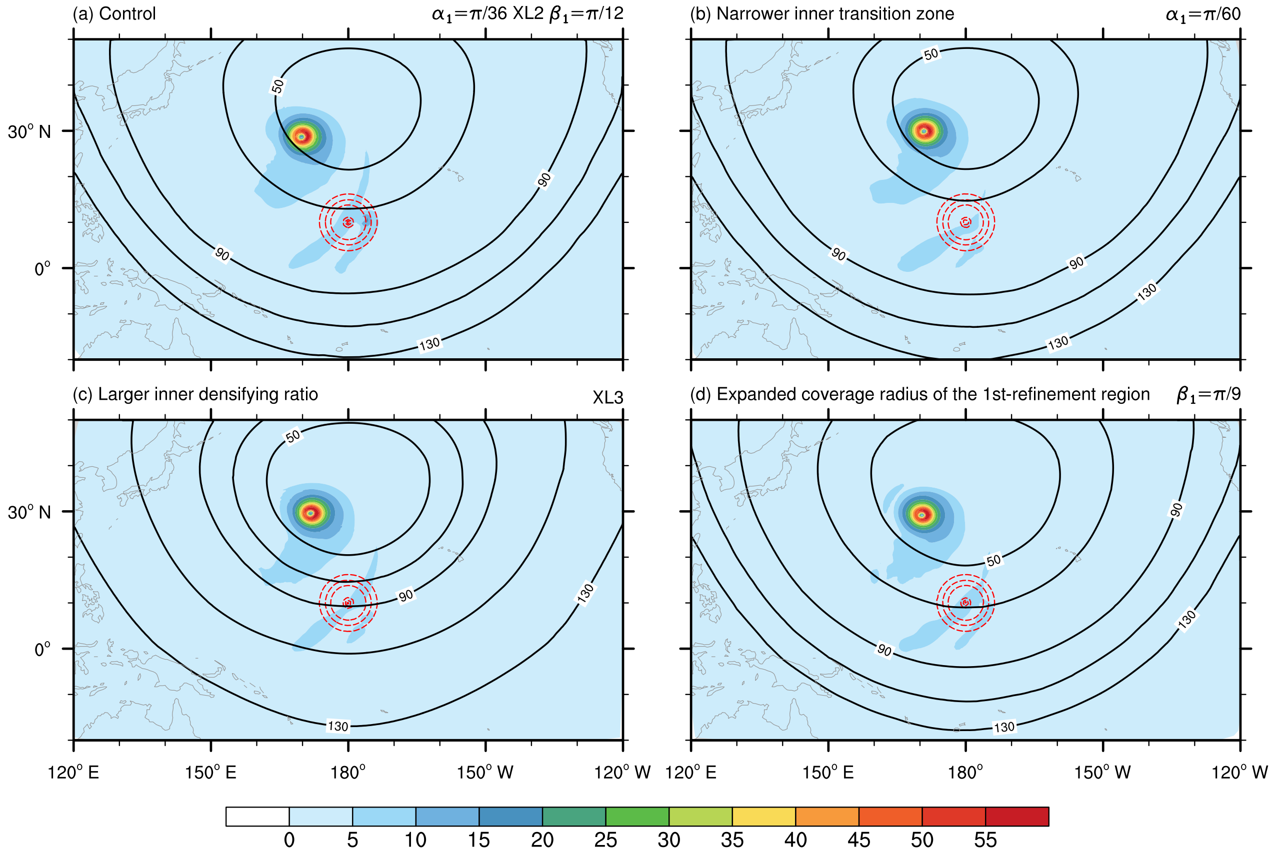

Figure 10: Idealized tropical cyclone test: the horizontal wind speed (m s^{-1}) at 850 hPa after 10 simulation days based on hierarchical refinement meshes with (a) the control, (b) reduced α_1, and (c) higher λ for more rapid changes in the transition zone, and (d) larger β_1 to make the transition zone affect the tropical cyclone in an earlier stage. The red dashes denote the initial location of the tropical cyclone. The contour lines denote the smoothed mesh cell sizes (km).

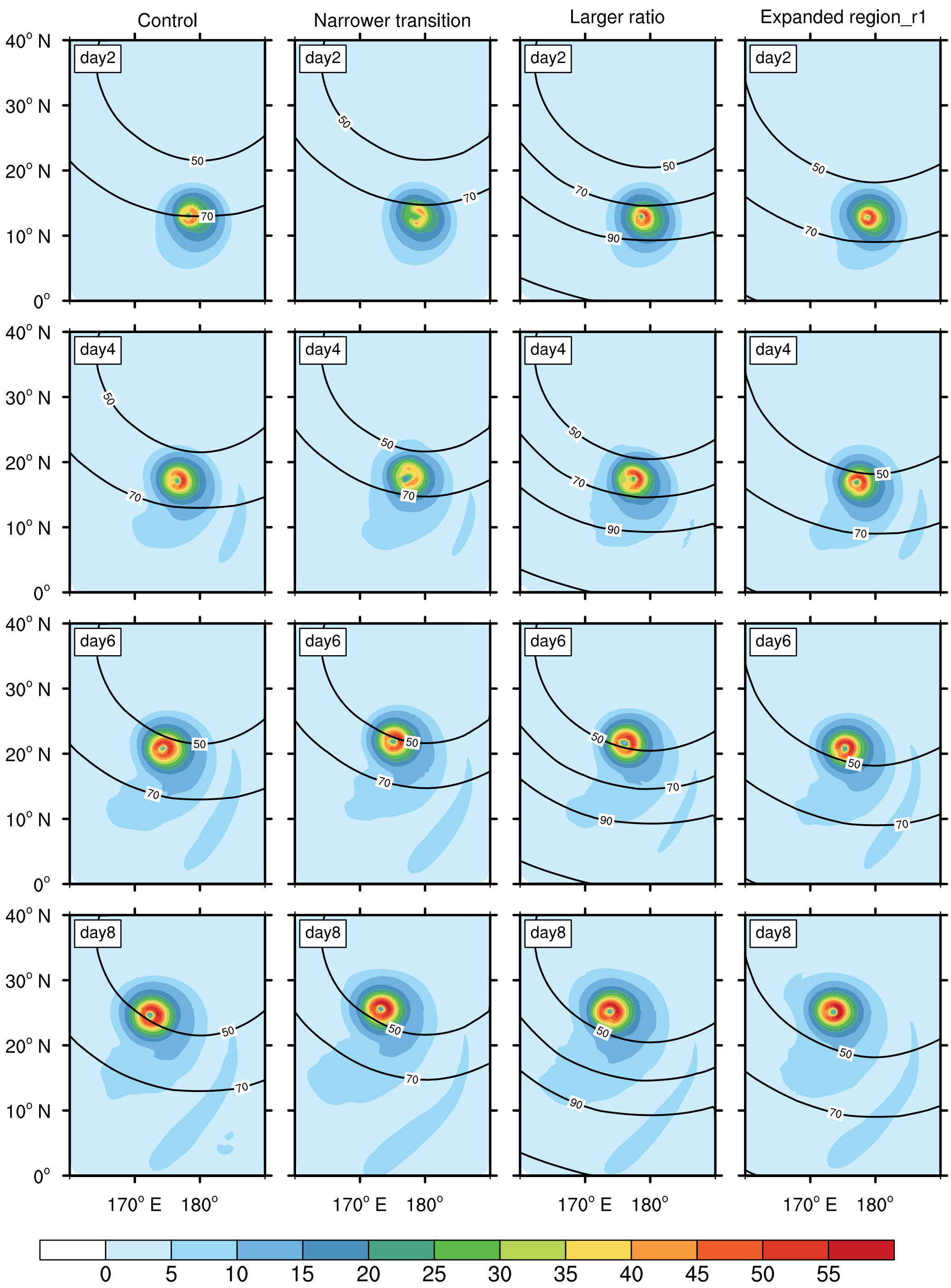

Figure 11: Corresponding to the four cases shown in Fig. 9, the simulation results on days 2, 4, 6, and 8 are shown to examine the movement of the tropical cyclones when they cross the mesh transition.

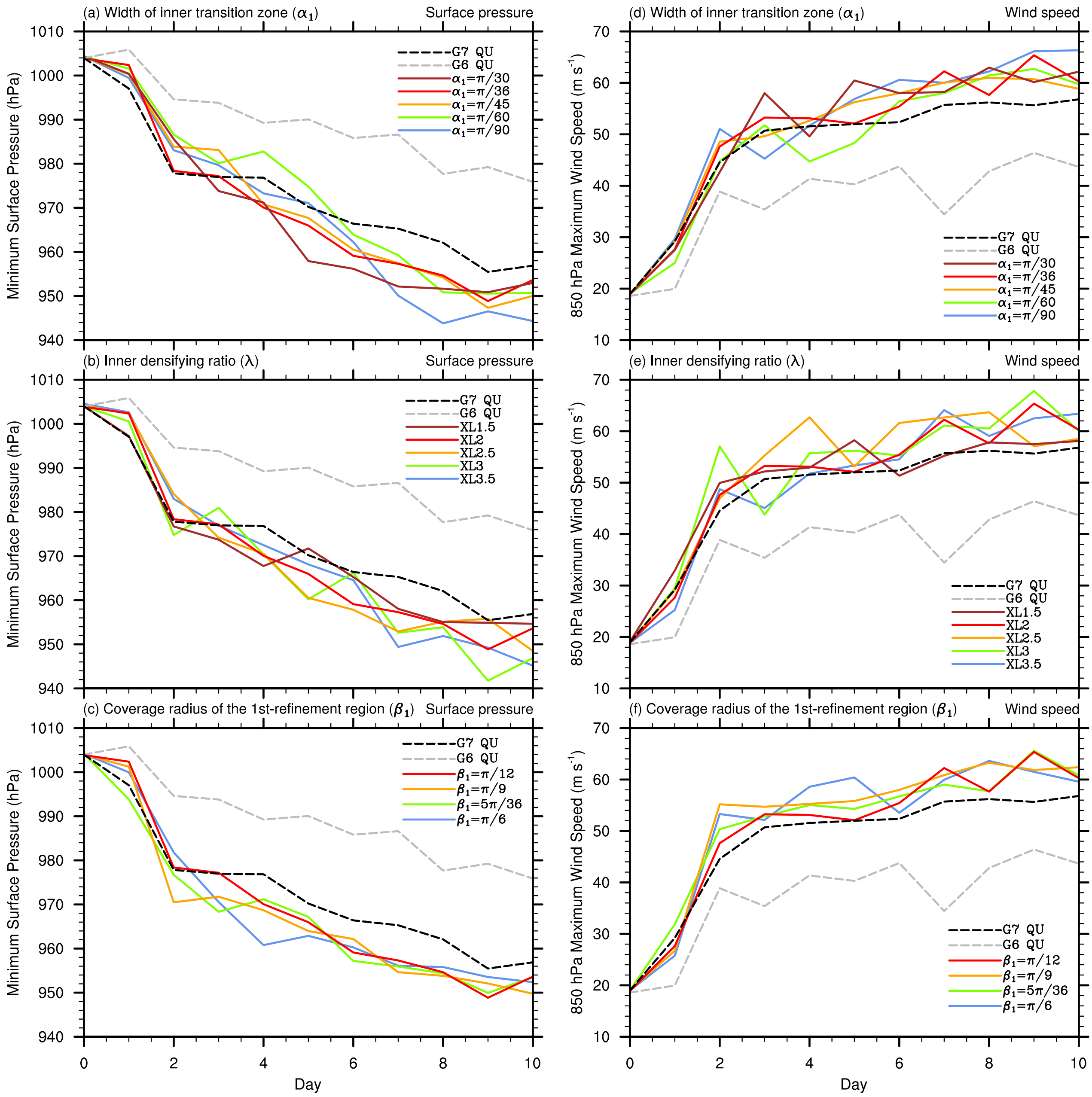

Figure 12 Idealized tropical cyclone test: temporal evolution of minimum surface pressure and maximum horizontal wind speed at 850 hPa based on the quasi-uniform G6 and G7 meshes, and the hierarchical refinement meshes by varying (a, d) α_1, (b, e) λ, and (c, f) β_1. When one parameter is altered, the other two parameters are fixed as in the control run ($\alpha_1 = \pi/36$, $\lambda = (1/2)^4$, and $\beta_1 = \pi/12$). The three mesh parameters control the width of the inner transition zone, the inner densification ratio, and the coverage radius of the 1st-refinement region.

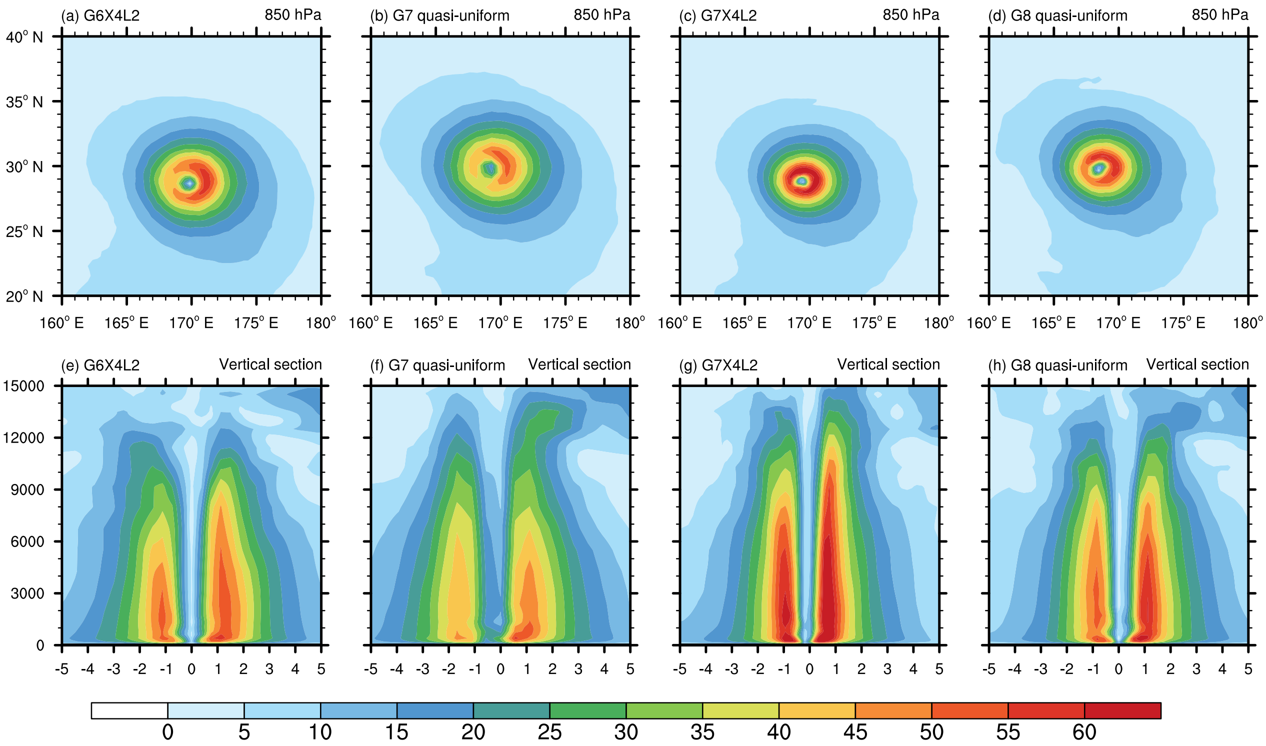

Figure 13: Idealized tropical cyclone test: (a–d) the horizontal wind speed (m s^{-1}) at 850 hPa after 10 simulation days based on quasi-uniform and variable-resolution meshes and (e–h) the corresponding vertical cross-section of the wind speed with a meridional range of ±5-degrees from the center of the tropical cyclone. The vertical coordinate of the cross-section denotes the height (m).

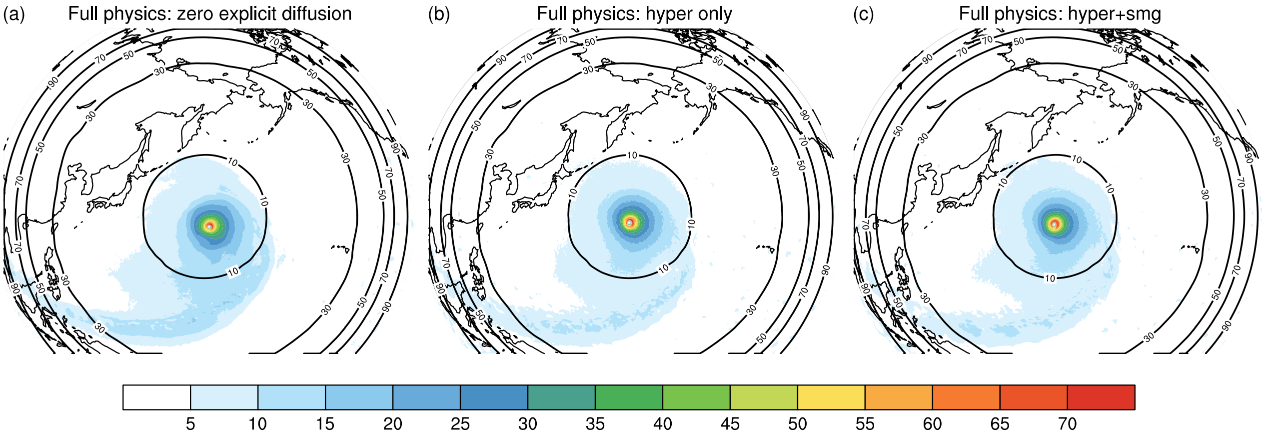

Figure 14 GRIST-NDC full physics tests with the G6B3X16L4 mesh: (a) no explicit diffusion is used, (b) only hyperdiffusion for the horizontal velocity is used, (c) both hyperdiffusion and Smagorinsky diffusion are used. The results are shown for the wind speed (m.s^{-1}) at the model level nearest to 850 hPa (level 24) on day 10. The contour lines denote the smoothed mesh cell sizes (km).

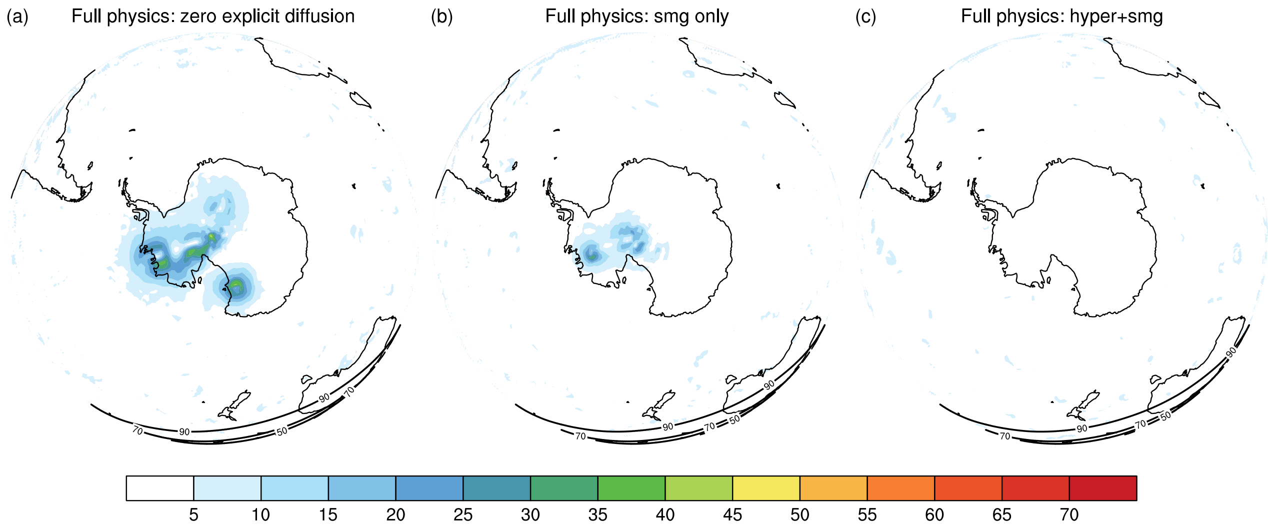

Figure 15: Same as Fig. 13, but the map is rotated to the South Pole.

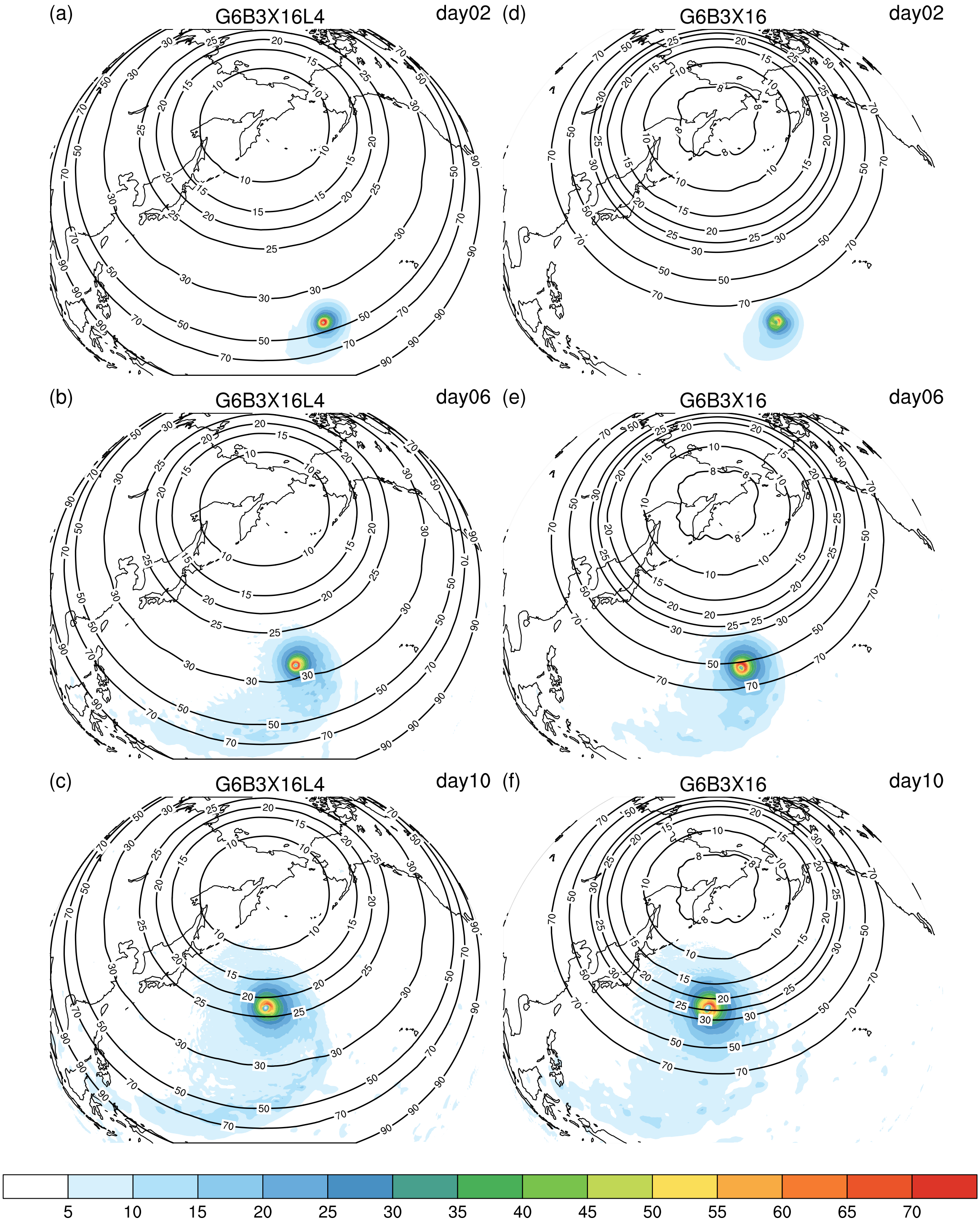

Figure 16: The same tests as in Fig. 13, but the refinement center is rotated to 60°N, 165°E. The left-hand column shows the results on days 2, 6, and 10 on the G6B3X16L4 mesh, the right-hand column shows the corresponding results on the G6B3X16 mesh. The results are shown for the wind speed (m.s^{-1}) at the model level nearest to 850 hPa (level 24).